

The Pennsylvania State University  
The Graduate School  
College of Earth and Mineral Sciences

**IMPACT OF ATOMIZATION AND PROCESSING GAS ON THE HEAT TREATMENT  
RESPONSE OF ADDITIVELY MANUFACTURED 17-4 PH STAINLESS STEEL**

A Thesis in  
Materials Science and Engineering  
by  
Scott D. Meredith

© 2018 Scott D. Meredith

Submitted in Partial Fulfillment  
of the Requirements  
for the Degree of  
Master of Science

December 2018

The thesis of Scott D. Meredith was reviewed and approved\* by the following:

Todd A. Palmer

Professor of Materials Science and Engineering

Professor of Engineering Science and Mechanics

Thesis Advisor

Allison M. Beese

Assistant Professor of Materials Science and Engineering

Reginald F. Hamilton

Associate Professor of Engineering Science and Mechanics

Jayme S. Keist

Research Associate of the Applied Research Laboratory at Penn State University

Special Signatory

Suzanne E. Mohny

Professor of Materials Science and Engineering and Electrical Engineering

Chair, Intercollege Graduate Degree Program in Materials Science and Engineering

\* Signatures are on file in the Graduate School.

## ABSTRACT

Precipitation hardened (PH) grade martensitic stainless steels are commonly used in additive manufacturing (AM) processes. In order to obtain properties similar to their wrought counterparts, post-processing solutionizing and aging heat treatments are required. Depending on the powder feedstock composition, which can be varied by the choice of atomization gas and, to a lesser extent, the processing gas during component fabrication, the post-process heat treatment response can be significantly altered. When the standard heat treatment cycles developed for wrought alloys are applied to as-deposited 17-4 PH grade stainless steel structures fabricated from argon or nitrogen atomized powder feedstocks on different powder bed fusion (PBF) systems, the AM components exhibited a difference response. Argon atomized feedstocks contain approximately 0.01 wt.% nitrogen, possess low levels of retained austenite, and respond as expected to standard solutionizing and aging heat treatment cycles. In contrast, 17-4 PH grade stainless steel structures fabricated using nitrogen atomized feedstocks with higher nitrogen levels (0.06 – 0.14 wt.%) and retained austenite levels (up to 81%) do not respond to standard solutionizing and aging techniques. Peak aging at these high nitrogen levels occurs at a temperature of approximately 680°C, which is significantly higher than the standard peak aging heat treatment at 482°C.

## TABLE OF CONTENTS

LIST OF FIGURES .....	vi
LIST OF TABLES .....	viii
ACKNOWLEDGEMENTS .....	ix
Chapter 1 INTRODUCTION.....	1
1.1 Background .....	1
1.2 Motivation .....	4
1.3 Objectives.....	4
1.4 Overview .....	4
Chapter 2 LITERATURE REVIEW.....	6
2.1 Impact of Alloying Elements .....	6
2.2 Impact of Austenite Retention on Precipitation Hardening .....	7
2.3 Powder Bed Fusion of 17-4 PH Stainless Steel .....	7
Chapter 3 ANALYSIS OF POWDER FEEDSTOCKS.....	10
3.1 Powder Feedstock Characterization Methods .....	10
3.2 Particle Morphology.....	12
3.3 Powder Flow Characteristics.....	15
3.4 Chemical Composition of the Powder Feedstocks.....	18
3.5 XRD Analysis of the Powder Feedstocks .....	18
3.6 Summary and Conclusions.....	23
Chapter 4 ANALYSIS OF AS-BUILT MATERIAL .....	26
4.1 Additive Manufacturing via Powder Bed Fusion.....	26
4.2 Chemical Composition of Fabricated Structures .....	26
4.3 XRD Analysis of Fabricated Structures .....	28

4.4 Computational Modeling of Phase Equilibria .....	28
4.5 Estimation of Martensite Start Temperature .....	29
4.6 Metallographic Analysis of Fabricated Structures .....	33
4.7 Summary and Conclusions.....	36
Chapter 5 ANALYSIS OF HEAT TREATED MATERIAL .....	38
5.1 Overview of Post-Fabrication Heat Treatments.....	38
5.2 Direct-Aging Heat Treatment.....	38
5.3 Two-stage Heat Treatment: Solutionizing Followed By Aging.....	41
5.4 Determination of Peak-Aging for Highly Austenitic Material.....	45
5.5 Three-stage Heat Treatment: Homogenization + Solutionizing + Aging .....	47
5.6 Summary and Conclusions.....	50
Chapter 6 SUMMARY .....	52
6.1 Primary Conclusions .....	52
6.2 Potential Next Steps .....	53
REFERENCES .....	54

## LIST OF FIGURES

Figure 1.1: Effect of cooling rate on ferrite/austenite boundaries of Schaeffler diagram [10] (adapted from David et al. [15]), with martensitic regions maintained for reference; dashed box indicates $Cr_{eq}$ and $Ni_{eq}$ limits calculated per specified composition of 17-4 PH stainless steel [3]	3
Figure 3.1: Micrographs of the four feedstock powders, including (a) argon atomized for the 3D Systems ProX 200, (b) nitrogen atomized for 3D Systems ProX 200, (c) argon atomized for EOS M280, and (d) nitrogen atomized for EOS M280 .....	10
Figure 3.2: Qualitative depiction of convexity and circularity parameters relative to the ideal value of unity .....	11
Figure 3.3: Volume-based Particle Size Distribution of the powder feedstocks, as measured by light-scattering (dashed line) and image analysis (solid line), for (a) ProX 200 and (b) EOS M280 .....	14
Figure 3.4: Image analysis results for the four powder feedstocks showing distributions of (a) convexity ratio and (b) circularity ratio .....	15
Figure 3.5: Accumulated charge versus time as measured by the REVOLUTION powder analyzer when powder is in contact with (a) glass or (b) polycarbonate.....	17
Figure 3.6: Comparison of XRD diffraction patterns of 3D Systems nitrogen atomized powder when scanned with or without a monochromator, both before and after software corrections ....	21
Figure 3.7: XRD patterns for AM 17-4 PH (a) feedstock and (b) in the as-built condition.....	24
Figure 4.1: Balmforth diagram [50] showing the standard chemical composition [3] for 17-4 PH stainless steel (delineated by a dashed box), as well as the position of the six AM builds, overlaid on a subset of the Schaeffler diagram [10].....	27
Figure 4.2: Equilibrium phase composition calculated as a function of temperature from the 3D Systems ProX 200 powder chemistries for (a) argon atomized and (b) nitrogen atomized feedstocks.....	30
Figure 4.3: Equilibrium phase composition calculated as a function of temperature from the EOS M280 powder chemistries for (a) argon atomized and (b) nitrogen atomized feedstocks.....	31
Figure 4.4: Simulated martensite start temperature as a function of nitrogen weight percent for each build composition .....	33
Figure 4.5: As-Built microstructures from (a) argon atomized feedstock for the 3D Systems ProX 200 processed under Ar atmosphere or (b) $N_2$ atmosphere; (c) argon atomized feedstock for EOS	

M280 (N <sub>2</sub> atmosphere); (d) nitrogen atomized feedstock for the ProX 200 processed under Ar atmosphere or (e) N <sub>2</sub> atmosphere; (f) nitrogen atomized feedstock for EOS M280 (N <sub>2</sub> atmosphere).....	35
Figure 4.6: EDS maps showing no observable elemental segregation for builds fabricated on the EOS M280 system from (a) argon atomized powder or (b) nitrogen atomized powder .....	36
Figure 5.1: Schematic of various heat treatment cycles, including (a) solutionizing for different durations, (b) aging directly from the as-built condition, (c) a two-stage heat treatment, and three-stage processes for which post-solution specimens were either (d) air-cooled or (e) water-quenched .....	39
Figure 5.2: Vickers hardness measurements compared to specification range for standard wrought materials when aged for 4 hours directly from the as-built condition for (a) 3D Systems ProX 200 and (b) EOS M280 system .....	40
Figure 5.3: Vickers hardness measurements following solutionizing at 1040°C for different durations, as compared to specified maximum for standard wrought materials, for (a) 3D Systems ProX 200 and (b) EOS M280 system .....	43
Figure 5.4: Vickers hardness measurements compared to specification range for standard wrought materials following two-stage heat treatment consisting of 30-min solutionization followed by 4-hour aging for (a) 3D Systems ProX 200 and (b) EOS M280 system .....	44
Figure 5.5: Elemental segregation of chromium and nickel observed in argon atomized material processed on the EOS M280, after solutionizing followed by aging at 620°C .....	45
Figure 5.6: Vickers hardness measurements of highly austenitic feedstock fabricated under nitrogen, then solutionized for either 30 or 60 min followed by 4-hour aging, with specified hardness range for H900 peak age condition [3] indicated by brackets .....	46
Figure 5.7: Comparison of austenite volume fraction and Vickers microhardness following a three-stage heat treatment consisting of homogenization, a solutionizing step that terminated in either air-cooling or a water-quench, then 4-hour aging; fabricated on 3D Systems ProX 200...	48
Figure 5.8: Comparison of austenite volume fraction and Vickers microhardness following a three-stage heat treatment consisting of homogenization, a solutionizing step that terminated in either air-cooling or a water-quench, then 4-hour aging; fabricated on EOS M280 .....	49
Figure 5.9: Comparison of austenite volume fraction and Vickers microhardness of highly austenitic feedstock fabricated on EOS M280, subjected to three-stage heat treatments.....	49

## LIST OF TABLES

Table 2.1: Limited chronology of previous work involving 17-4 PH stainless steel fabricated by powder bed fusion.....	8
Table 3.1: Powder characterization data, including morphological and flow properties .....	13
Table 3.2: REVOLUTION powder analyzer dynamic flowability results .....	16
Table 3.3: Chemical compositions of powder feedstocks and fabricated builds, with corresponding austenite volume fractions .....	19
Table 3.4: Ni equivalent and Cr equivalent weight fractions per Balmforth constitution diagram as calculated from chemical compositions for each feedstock and AM build, as well as volume fraction of retained austenite as measured by XRD.....	20
Table 3.5: Summary of parameters used to analyze x-ray diffraction data for determination of retained austenite volume fractions .....	22
Table 4.1: Summary of phase equilibrium temperatures and Scheil solidification calculations computed from the chemical compositions of the four powder feedstocks.....	32
Table 5.1: Comparison of austenite volume fraction and Vickers microhardness after 4-hour aging directly from the as-built condition.....	40
Table 5.2: Comparison of austenite volume fraction and Vickers microhardness after solutionizing at 1040°C for different durations .....	43
Table 5.3: Comparison of austenite volume fraction and Vickers microhardness after 30-min solutionizing heat treatment at 1040°C followed by 4-hour aging; fabricated on 3D Systems ProX 200 .....	44
Table 5.4: Comparison of austenite volume fraction and Vickers microhardness for various 4-hour aging heat treatments following a 30-min or 60-min solutionizing step for nitrogen atomized material processed on the EOS M280 system.....	46
Table 5.5: Comparison of austenite volume fraction and Vickers microhardness following a three-stage heat treatment consisting of homogenization, a solutionizing step that terminated in either air-cooling or a water-quench, then 4-hour aging; fabricated on 3D Systems ProX 200...	48
Table 5.6: Comparison of austenite volume fraction and Vickers microhardness following a three-stage heat treatment consisting of homogenization, a solutionizing step that terminated in either air-cooling or a water-quench, then 4-hour aging; fabricated on EOS M280 .....	50



## ACKNOWLEDGEMENTS

I wish to extend my sincerest gratitude to my advisor, Dr. Todd A. Palmer, for allowing me this opportunity to resume my education in a new field. The patience, guidance, and wisdom provided by both Dr. Palmer and Dr. Jay Keist were invaluable in developing my fundamental understanding of metallurgy and materials science. As a member of TeamTAP, it was my great privilege to collaborate with and learn from my fellow group members: Zakariya Khayat, Marissa Brennan, and Andrew Iams. Their diligence, positivity, and thoughtfulness represented a constant source of inspiration as well as a target for aspiration.

I also wish to acknowledge some of the many individuals who assisted me these past few years. I am immensely grateful for the contribution of James Zuback, whose thermodynamic modeling greatly enhanced the results of this study. Thank you to my thesis committee members, Dr. Allison Beese and Dr. Reginald Hamilton, who have been gracious in sharing not only their knowledge, but also access to their groups' resources! Thank you to the incredible personnel affiliated with Penn State's Center for Innovative Materials Processing through Direct Digital Deposition (CIMP-3D), including Barbra Belko, Ed Good, Jay Tressler, Griffin Jones, Corey Dickman, Dr. Ken Meinert, and Jared Blecher of 3D Systems, Inc. Thanks to Julie Anderson, Nichole Wonderling, and Gino Tambourine for their tremendous patience as they initiated new users like myself to the equipment at the Materials Characterization Lab. Additional thanks go to Nicholas Carrier for providing SEM of the powders and Evan McHale for contributing some of the XRD scans.

I will forever be indebted to my family and friends for their unwavering support and encouragement. In addition, I'd like to express appreciation to my former colleagues Andrew Albanese, Roland Roberge, Greg Smith, Joe Pellock, Gene Mancini, Charles Hinchman, Edward Bommarito, and Gary Johnson for their mentorship and contributions toward my personal and professional development.

Finally, financial support from the Cross Platform System Development (CPSD) program and Naval Sea Systems Command (NAVSEA) contract #N00024-12-D-6404 is gratefully recognized.

## Chapter 1

### INTRODUCTION

#### 1.1 Background

Precipitation-hardened (PH) martensitic grade stainless steels are widely used in aerospace, marine, chemical, food processing, power generation, and paper industries. [1,2] In addition to the hard martensitic matrix, strengthening is derived through the formation of sub-micron copper-rich precipitates during post-process aging heat treatments. The temperature and duration of these heat treatments, which follow a solutionizing heat treatment, can be adjusted to produce a range of strength levels. [3] In the peak-aged or H900 condition (1 hr, 482°C) [3], the elliptical Cu-rich precipitates are approximately 25 nm in length. [4] As the material is aged at higher temperatures or longer times, a minimization of surface energy leads to Ostwald ripening and an increase in the size of the precipitates. [5] The diminishing number of precipitates, loss of coherency with the matrix, and tempering of the martensitic matrix during these overaging cycles causes a decline in mechanical strength but an improvement in other properties such as ductility and impact toughness. [2]

The weldability of the 17-4 PH alloy system makes it an excellent candidate for additive manufacturing (AM) processes. [6] Unlike alloys that initially solidify as austenite (A or AF), the primary ferritic solidification mode (F) of 17-4 PH stainless steel [7,8] increases its resistance to welding issues such as solidification cracking. [9] Various diagrams have been developed to predict the solidification mode as a function of composition. For example, the Schaeffler diagram [10] determines chromium and nickel equivalents using the following relationships (all concentrations in weight percent):

$$Cr_{eq} \text{ (wt.\%)} = [Cr] + [Mo] + 1.5 \times [Si] + 0.5 \times [Nb] \quad (1)$$

$$Ni_{eq} \text{ (wt.\%)} = [Ni] + 30 \times [C] + 0.5 \times [Mn] \quad (2)$$

Vulnerability to solidification cracking has been shown to increase sharply as the  $Cr_{eq}/Ni_{eq}$  ratio falls below a critically low level [9,11] approximated in the range of 1.49 to 1.84 [11–13]. Applying the Schaeffler equations to the specified chemical composition of UNS S17400 grade stainless steel [3] yields a Cr/Ni equivalency ratio in the range of 2.0 to 6.4, sufficiently above this threshold. Although higher  $Cr_{eq}/Ni_{eq}$  values can also increase

susceptibility to solidification cracking [9,11], the F solidification mode still remains superior to a primarily austenitic solidification mode. [9]

In addition to chemistry, microstructural development can also be influenced by cooling rate. [14–17] For example, rapid solidification techniques such as splat quenching [14], laser welding [14,15], and electron beam melting [16] have all produced results that are inconsistent with the Schaeffler diagram. Though Ni-rich alloys ( $\text{Ni}_{\text{eq}} > 19$ ) maintained a fully austenitic (A) solidification mode, different ferrite levels as a function of cooling rate were observed for alloys with  $\text{Cr}_{\text{eq}}/\text{Ni}_{\text{eq}} \geq 1.4$  by altering the scanning speed [14–16] or power level [15] of the energy beam. While alloys within the austenite-ferrite region may exhibit a duplex solidification mode (AF or FA) at slow to moderate cooling rates, compositions near the single-phase boundaries were more likely to exhibit single phase solidification modes (A or F) at rapid cooling rates. [14–16] The proposed mobility of the austenite-ferrite boundaries within the Schaeffler diagram as function of cooling rates estimated by calculation is depicted in Figure 1.1. [15]

The rapid scanning rates of high energy sources like those associated with additive manufacturing generally lead to a refined grain structure. [18] Powder bed fusion (PBF) systems in particular employ rapid scanning rates along narrow melt pools corresponding to high cooling rates. [17] Fine austenite grains ( $< 20 \mu\text{m}$  in size) have been shown to inhibit martensitic transformation [19,20], contributing to higher austenite retention.

The cooling rate for austenitic stainless steel in a laser powder bed fusion (PBF) process has been reported to be on the order of  $10^5$  to  $10^6$  K/s. [21] Cooling rates of this magnitude are also comparable to production of 17-4 PH powder feedstocks via gas atomization, with rates increasing to  $10^7$  K/s for particle diameters smaller than 10 microns. [22] During gas atomization, a high velocity gas is directed into a superheated molten stream of the alloy to disintegrate it into fine droplets, which then minimize surface energy by reforming into spheres prior to solidification. [23]

While nitrogen is a less expensive atomization gas than argon, its impact on alloy chemistry must also be considered. Due to the strong austenite stabilizing effect of nitrogen [24], moderate changes can have a profound impact on the microstructural constituents of 17-4 PH stainless steel. The combination of residual nitrogen from gas atomized feedstocks with the refined grain structure yielded by the PBF process promotes higher levels of retained austenite.

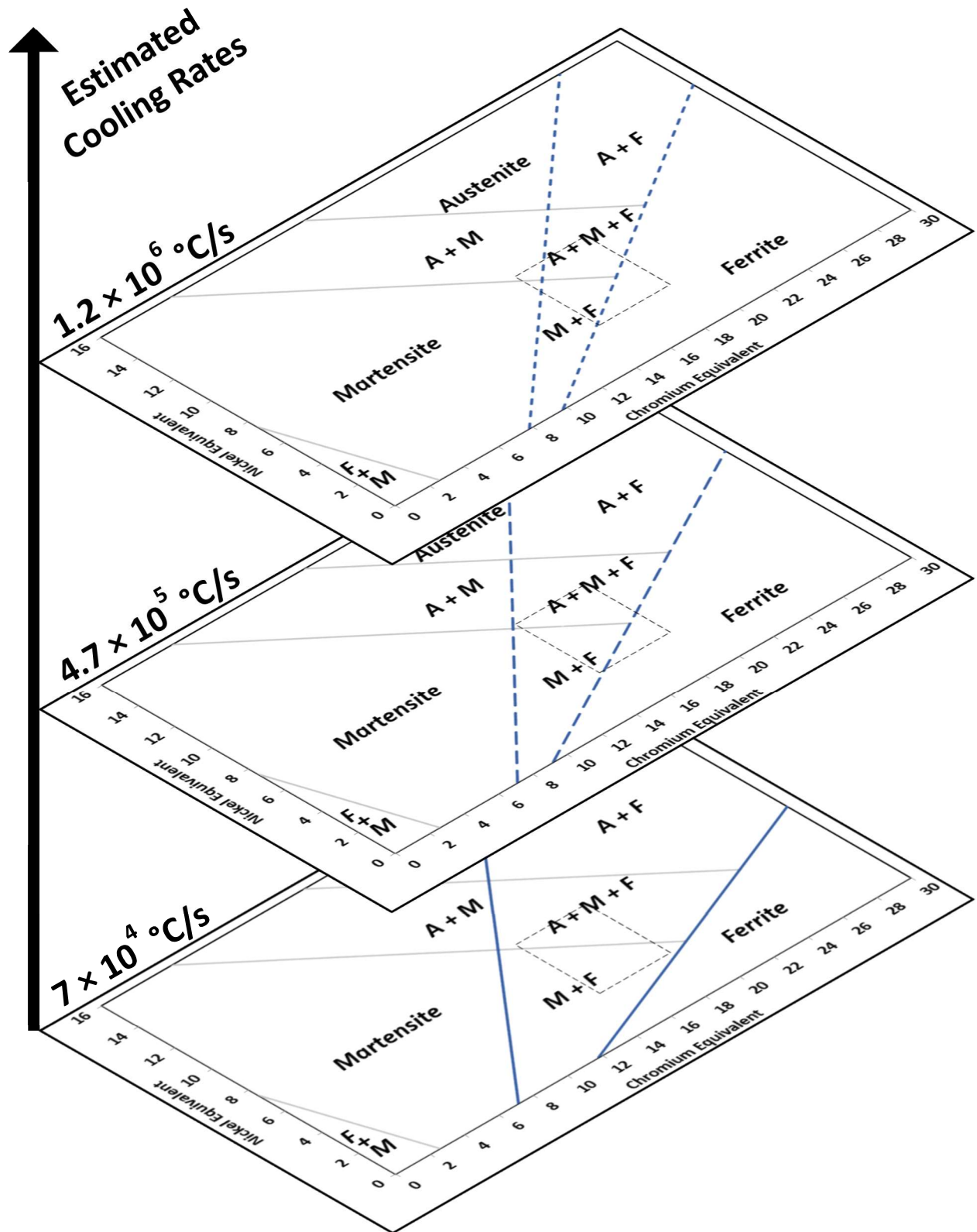


Figure 1.1: Effect of cooling rate on ferrite/austenite boundaries of Schaeffler diagram [10] (adapted from David et al. [15]), with martensitic regions maintained for reference; dashed box indicates  $\text{Cr}_{\text{eq}}$  and  $\text{Ni}_{\text{eq}}$  limits calculated per specified composition of 17-4 PH stainless steel [3]

As will be discussed in subsequent chapters, these variations in austenite retention affect the heat treatment response of AM 17-4 PH stainless steel.

## **1.2 Motivation**

Variations in feedstock chemical composition, in conjunction with the rapid cooling associated with PBF processes, produce microstructures that differ from conventional wrought material. Although nitrogen concentration can be influenced by the choice of atomizing gas, ASTM standards for the 17-4 PH stainless steel grade currently do not include a specification for nitrogen content. The purpose of this work is to show how solidification pathways are influenced by composition, highlight the strong austenite-stabilizing effect of nitrogen, and understand how these variations impact the overaged heat treatment response of the alloy.

## **1.3 Objectives**

Four powder feedstocks representing a range of chemical compositions were additively manufactured under either a nitrogen or argon atmosphere, and then subjected to a series of post-process heat treatments to achieve the following goals:

- To illustrate how chemical composition, particularly nitrogen, impacts the amount of retained austenite within additively manufactured 17-4 PH stainless steels
- To investigate how variations in austenite levels influence the hardening response of the alloy through a series of overaging heat treatments
- To demonstrate the effect of homogenization and solutionizing heat treatments on the overage response
- To identify a potential heat treatment path that achieves the peak-aged condition in highly austenitic AM components of 17-4 PH stainless steel

## **1.4 Overview**

The body of this work is divided into six chapters.

The purpose of Chapter 1 is to provide an introductory background on the topic and convey the scope of the work.

Chapter 2 provides a review of previous studies involving the powder bed fusion of 17-4 PH stainless steel and subsequent post-processing heat treatments.

In Chapter 3, the four powder feedstocks acquired for this study are compared on the basis of particle morphology, flowability, chemistry, as well as the proportions of primary phases present.

Chapter 4 focuses on the as-built condition of the additively manufactured components, relating theoretical modeling of solidification and phase transformations to the respective chemical compositions and measured phases.

Chapter 5 presents the impact of various post-processed heat treatment paths, including single stage (aging directly from the fabricated condition), two-stage (solutionization followed by aging), and three-stage heat treatments (addition of an initial homogenization step).

Finally, Chapter 6 summarizes the work by highlighting the primary conclusions and discussing potential future work.

## Chapter 2

### LITERATURE REVIEW

#### 2.1 Impact of Alloying Elements

The selection of atomization gas can affect the nitrogen content of the powder feedstock. However, the solubility of nitrogen in ferrous alloys depends upon the temperature of the melt as well as its composition. [25] Certain elements (Ni, C, P, Si, S) reduce nitrogen solubility whereas a combination of chromium and manganese increases it. [25–28]

While elements like carbon and nitrogen strongly favor austenite retention [28], the interaction between chromium and manganese is more complicated. At very low concentrations, such as that found in 17-4 PH stainless steel, manganese is also a slight austenitizer. [29] However, the austenite stabilizing ability of manganese diminishes as the concentration increases to the 5-8 % range [29], and actually becomes a ferrite stabilizer above 12 % [27], while also increasing the ferrite-stabilizing effect of chromium. [30] Conversely, as chromium content increases to 18-23%, manganese can become a ferrite stabilizer at concentrations as low as 0.5wt.%. [29,31] Therefore, the impact of manganese is partially determined by the chromium content. Another important effect of chromium is that it promotes martensitic transformation by lowering the stacking fault energy. [32]

While the Schaeffler constitution diagram [10] serves as a guide to predict solidification, a well-known deficiency is that it does not account for the strong austenite-stabilizing effect of nitrogen. Many alternative equivalency equations have been proposed over time, such as those developed in 2000 for the ferritic-martensitic region (applicable to  $Ni_{eq}$  values up to 8) using a conventional arc welding process, with the weight factors shown in equations (3) and (4):

$$Cr_{eq} \text{ (wt.\%)} = [Cr] + 2 \times [Mo] + 10 \times [Al] + 10 \times [Ti] \quad (3)$$

$$Ni_{eq} \text{ (wt.\%)} = [Ni] + 35 \times [C] + 20 \times [N] \quad (4)$$

Equation (4) demonstrates the strong impact of nitrogen on nickel equivalency, yet no range for nitrogen is listed among the specified chemical composition for 17-4 PH stainless steel. [3,33] Therefore, any manufactured lot that otherwise satisfies the alloy's chemical requirements could possess higher than expected nickel equivalency values.

## 2.2 Impact of Austenite Retention on Precipitation Hardening

In addition to being softer than martensite [34], higher levels of retained austenite impact the precipitation kinetics in 17-4 PH grade stainless steel. [35] The primary precipitating species, copper, has a much higher solubility and lower diffusivity in austenite compared to ferrite, so increased levels of austenite disrupts the normal heat treat response. [35–37] Peak aging can still be achieved in the presence of significant amounts of retained austenite, but higher temperatures are required for sufficient diffusion to occur.

## 2.3 Powder Bed Fusion of 17-4 PH Stainless Steel

Table 2.1 presents a limited summary of previous studies involving 17-4 PH stainless steel fabricated via powder bed fusion. Some of the earliest observations of high levels of retained austenite associated with additively manufactured 17-4 PH stainless steel were published in 2010. [38,39] While Facchini et al. [38] attributed the 72% austenite to the rapid cooling rates, Averyanova et al. [39] noted the impact of chemical composition by comparing powders with different nickel and chromium contents. However, neither commented on the role of nitrogen.

The impact of nitrogen would be revealed in contemporaneous studies around 2012, which varied the gas used in the atomization of the feedstock and the PBF atmosphere between argon or nitrogen. [34,40] While the majority of the builds of the test matrix resulted in the conventional martensitic structure, in both cases the combination of a nitrogen atomized powder processed under a nitrogen atmosphere (henceforth abbreviated as  $N_2/N_2$ ) was found to be more austenitic. Both studies also noted phase disparities in the feedstock itself, with the argon atomized powder being martensitic while the nitrogen atomized powder consisted of primarily austenite, with Starr et al. [40] reporting that the latter contained five times the nitrogen content, but the concentrations of other alloying elements were not revealed. Following an H900 peak-aging heat treatment (482°C for 1 hr) [3] directly from the as-built condition, Murr et al. [34] observed an increase in hardness for the martensitic builds, but the  $N_2/N_2$  condition exhibited little change in hardness upon aging.

In 2014, Rafi et al [7] similarly observed a higher proportion of retained austenite in the as-built product when nitrogen atomized material was processed under nitrogen versus argon. Although an initial heat treatment (788°C, 2 h) raised the yield strength and ultimate



Table 2.1: Limited chronology of previous work involving 17-4 PH stainless steel fabricated by powder bed fusion

	Feedstock Atomization	AM Shield Gas	Reported Chemistry	Heat Treatment(s)
2010, Facchini et al. [38]	Ar	Ar	N not reported	• stress-relief (SR) only
2010, Averyanova et al.[39]	(gas)	Ar	N, Mo not reported	[none]
2012, Murr et al. [34]	Ar vs N <sub>2</sub>	Ar vs N <sub>2</sub>	ranges reported	• peak-aging (1h, 482°C)
2012, Starr et al. [40]	Ar vs N <sub>2</sub>	Ar vs N <sub>2</sub>	only N, O reported	• SR (650°C) vs SR (788°C)
2014, Rafi et al. [36]	N <sub>2</sub>	N <sub>2</sub>	only N reported	• SR (650°C) vs SR (788°C) • SR (788°C) + peak-aging (1h, 482°C)
2015, Cheruvathur et al. [41]	N <sub>2</sub>	N <sub>2</sub>	N not reported <sup>1</sup>	• SR (650°C) vs solutionizing (1h, 1050°C) vs homogenization (2h, 1150°C) • homogenization + solutionizing (0.5h, 1050°C)
2015, LeBrun et al. [37]	Water	N <sub>2</sub>	N, Mo not reported	• aging (1h, 482°C; 4h, 550°C; 4h, 620°C) • solutionizing (0.5h, 1040°C) + aging (1h, 482°C; 4h, 550°C; 4h, 620°C)
2017, Mahmoudi et al. [6]	(gas)	N <sub>2</sub>	ranges reported	• solutionizing (0.5h, 1040°C) + peak-aging
2017, Clausen et al.[43]	N <sub>2</sub>	N <sub>2</sub>	(complete)	• SR (1h, 650°C) under vacuum (~10 <sup>-6</sup> Torr)

<sup>1</sup> Chemistry, including nitrogen, for AM material fabricated from the same feedstock later reported in 2017 by Stoudt et al. [42]

tensile strength compared to the as-built condition, once again no hardening effect was observed following a subsequent peak-aging heat treatment. Although no aging treatments were considered for a study by Cheruvathur et al. [41] involving as-built N<sub>2</sub>/N<sub>2</sub> material containing 50% austenite, their work likewise showed an increased hardness when subjected to the standard “Condition A” [3] solution heat treatment (1050°C, 1 h), and to a lesser extent following a two-stage heat treatment of homogenization (1150°C, 2 h) [44] plus solutionizing (1050°C, 0.5 h).

In addition to H900 peak-aging, LeBrun et al. [37] included H1025 and H1150 [8] overaged conditions in their work. Samples fabricated from water-atomized powder feedstock under a nitrogen atmosphere were aged directly from the as-built condition and were then compared to the same set of aging treatments following an initial solutionizing step (1050°C, 0.5 h). The results showed varying degrees of retained and reverted austenite, as well as how aging directly from the as-built condition can result in mechanical properties that deviate from the typical downward progression associated with overaging.

These previous studies have demonstrated that the standard heat treatments developed for martensitic wrought materials do not elicit the same response when applied to AM 17-4 PH stainless steel, due to increased levels of retained austenite within the AM components inhibiting precipitation kinetics. Although the presence of austenite was partially attributed to nitrogen (introduced either by the atomization gas of the feedstock or by the AM shielding gas), as noted in Table 2.1, complete chemistries were seldom reported. This study provides elemental analysis for both the feedstock and AM builds, to quantify the impact that atomization and processing conditions have on the chemical composition, and to further investigate the role that composition has on austenite retention in AM components. Also, while much of the previous work has focused on the peak-aged condition [6,34,36,37] (often omitting the standard solution heat treatment) [34,36], this study explores the heat treat response among different overage conditions, both directly from the as-built condition and as part of multi-stage heat treatments consisting of homogenization and solutionizing. Additional non-standard heat treatments were conducted to identify the peak-aged condition for highly austenitic AM 17-4 PH, which required 4 hours at 680°C.

### 3.1 Powder Feedstock Characterization Methods

Four powder feedstocks that satisfied the chemical requirements for 17-4 PH stainless steel [3] were obtained from different vendors<sup>2,3,4,5</sup>, including two argon-atomized powders and two nitrogen-atomized powders to ensure a range of nitrogen compositions. The original equipment manufacturer feedstocks for both the 3D Systems ProX 200 and EOS M280 PBF systems were nitrogen atomized. Powder chemistries were measured by a certified lab<sup>6</sup> using LECO combustion analysis per ASTM E1019-11 [45] for the elements C, S, O, and N, and inductively coupled plasma atomic emission spectroscopy (ICP-AES) in accordance with ASTM E1479-16 [46] for the remainder of the elements. Figure 3.1 shows secondary electron (SE)

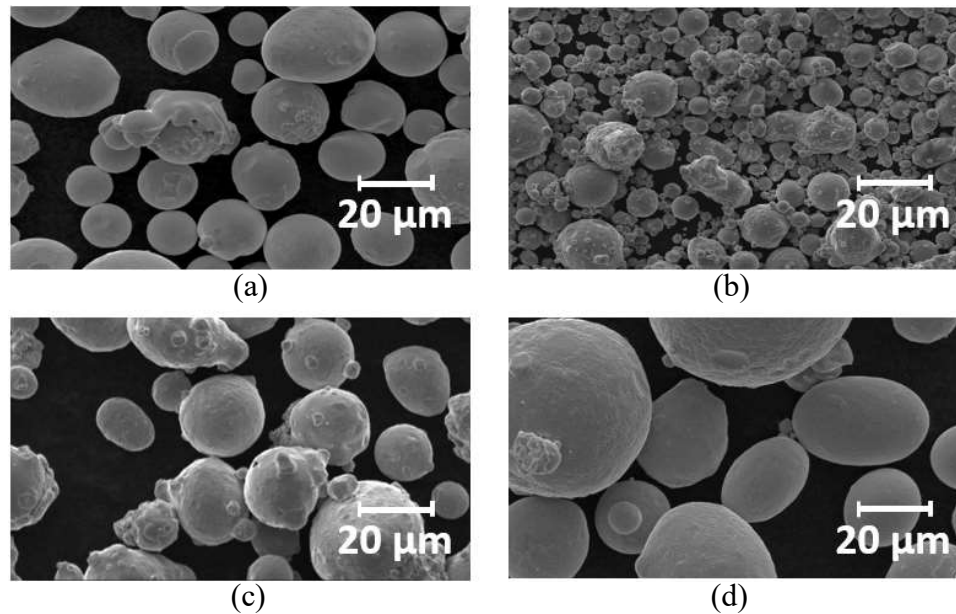


Figure 3.1: Micrographs of the four feedstock powders, including (a) argon atomized for the 3D Systems ProX 200, (b) nitrogen atomized for 3D Systems ProX 200, (c) argon atomized for EOS M280, and (d) nitrogen atomized for EOS M280

<sup>2</sup> Phenix Systems, a subsidiary of 3D Systems, Inc; Rock Hill, SC

<sup>3</sup> Praxair Surface Technologies; Indianapolis, IN

<sup>4</sup> EOS (Electro Optical Systems) of North America, Inc; Novi, MI

<sup>5</sup> LPW Technology, Inc; Imperial, PA

<sup>6</sup> Westmoreland Testing & Research, Inc; Youngstown, PA

images of the powders, captured by a Philips XL-30 Environmental Scanning Electron Microscope.

The powders were characterized using conventional methods typically applied in powder metallurgy, as well as more modern instrumentation. Flowability was measured using a standard Hall funnel [47], and was then combined with a 25 cm<sup>3</sup> brass cup [48] to determine apparent density. At least three measurements for each powder were performed to calculate average values. Since all of the powders exhibited a “no flow” condition, flow was assisted by continuous agitation of the powder to generate results for relative comparisons. The average tap density [49] was also calculated from three measurements, after the powder had been settled by at least 3000 cycles on a QuantaChrome Dual Autotap model DA-1.

Particle size distributions of the powders were assessed by a Malvern Mastersizer 2000 light scattering technique. Image analysis was also performed using a Malvern Morphologi® G3, which is capable of providing additional information on particle shape. For example, convexity ratios offer an indication of surface roughness by comparing convex hull perimeters of two-dimensional profiles of the particles to their actual perimeters. The convex hull perimeter is determined by encasing the particle profile within a convex polygon, in which straight lines connect the farthest-protruding peaks extending from the particle surface. A circularity parameter simultaneously describes both surface roughness and shape by converting the area of the two-dimensional profile to a circular equivalent (CE) diameter, and then calculating the ratio of the CE diameter to the actual perimeter. As depicted in Figure 3.2, for an ideal spherical

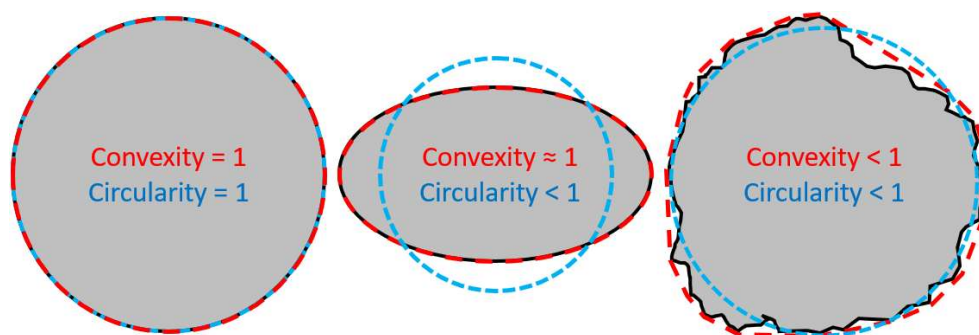


Figure 3.2: Qualitative depiction of convexity and circularity parameters relative to the ideal value of unity

particle with a perfectly smooth and circular profile, both the convex hull (shown as red broadly spaced dashed lines) and circular equivalent diameter (shown as blue finely spaced dashed lines) match the actual particle perimeter. If, however, the shape is distorted while still maintaining a smooth surface, the convexity remains close to the ideal value of unity but the circularity ratio decreases. As both surface roughness and shape continue to deviate from the ideal profile, the convexity and circularity values both decline.

The flowability of the powders was further assessed using the REVOLUTION powder analyzer<sup>7</sup>. A translucent sample drum is charged with 100 cubic centimeters of powder and loaded into the instrument between a backlight and a camera. The pixel heights corresponding to the silhouette produced by material blocking out the backlight are converted into potential energy; as the drum rotates, the changing profile of the powder can then be monitored and evaluated as changes in energy. For example, break energy is defined as the average maximum potential energy of the powder, before gravity overcomes the interparticle friction and results in an avalanche. Higher break energy indicates a greater resistance to flow. Avalanche energy represents the decline in potential energy following the change in profile. With the addition of the ION Charge Module, the tribocharging properties of the powders were also assessed. The drum was rotated at a rate of 10 rpm for a duration of 60 seconds, and then any decay in charge was also monitored for up to 30 seconds after rotation was terminated.

### 3.2 Particle Morphology

As observed in the micrographs shown in Figure 3.1, the particle sizes of the feedstocks for the 3D Systems ProX 200 are slightly smaller than those for the EOS M280 system. This is verified by the D<sub>10</sub>, D<sub>50</sub>, and D<sub>90</sub> values listed in Table 3.1, as well as full plots of the normalized particle size distributions shown in

(b)

Figure 3.3. The Malvern Morphologi G3 classified the particles into 1000 size bands, spaced logarithmically, while an order of magnitude fewer bands applied to the Mastersizer scans resulted in smoother curves with lower resolution.

---

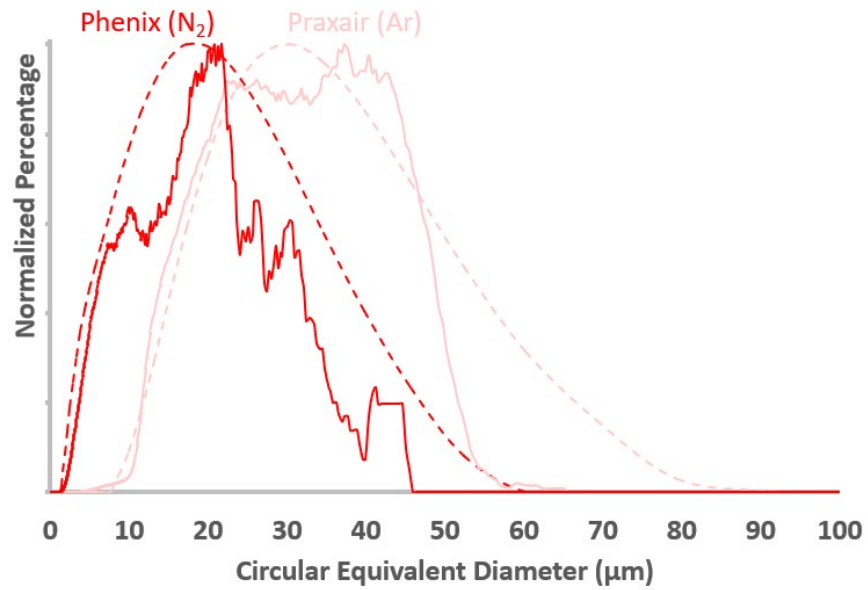
<sup>7</sup> Mercury Scientific Inc.; Newtown, CT

The consistent spherical morphology produced by the gas atomization process is evident in Figure 3.4, which displays percentage distributions of convexity and circularity ratios for each of the four powders. The surface roughness of the two feedstocks acquired for the EOS M280 system, as measured by the convexity ratio, were similar, but a greater proportion of the nitrogen atomized powder exhibited more ideal circularity. The superior results for the 3D Systems nitrogen atomized powder—particularly the low surface roughness—are likely inflated due to the fine particle size limiting the ability to resolve deviations within the profiles. This exacerbated the perceived difference from the corresponding argon atomized powder, for which more than 95% of the analyzed particles still had a convexity ratio of at least 0.8.

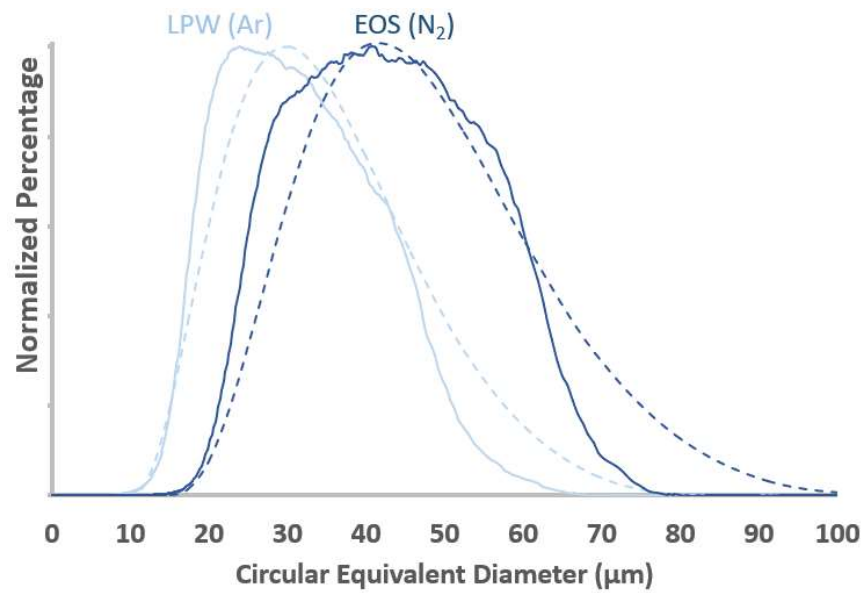
Table 3.1: Powder characterization data, including morphological and flow properties

		3D Systems ProX 200		EOS M280	
		Ar atomized	N <sub>2</sub> atomized	Ar atomized	N <sub>2</sub> atomized
PSD (Vol. basis)	D <sub>10</sub> (μm)	15	4	17	26
	D <sub>50</sub> (μm)	27	13	28	29
	D <sub>90</sub> (μm)	47	30	44	58
Image Analysis	# Particles Analyzed	94,115	95,072	228,574	81,235
	Mean Convexity	0.936	0.992	0.983	0.950
	Mean Circularity	0.909	0.969	0.944	0.982
Apparent Density (g/cm <sup>3</sup> )		3.95	2.72	3.45	3.83
Tap Density (g/cm <sup>3</sup> )		5.0	4.7	4.5	5.1
Hausner ratio ( $\rho_T/\rho_A$ )		1.27	1.73	1.30	1.33
Hall Flow Rate* (sec/50 g)		24.8	290.2	12.3	24.5
Angle of Repose ( $\pm 0.5^\circ$ )		25.5°	51.5°	27.5°	35.0°

*(\*Note: standard Hall flow method resulted in “no flow” condition for all powders; the listed flow times correspond to continuous agitation of the powder and should be considered for relative comparisons only)*



(a)



(b)

Figure 3.3: Volume-based Particle Size Distribution of the powder feedstocks, as measured by light-scattering (dashed line) and image analysis (solid line), for (a) 3D Systems ProX 200 and (b) EOS M280

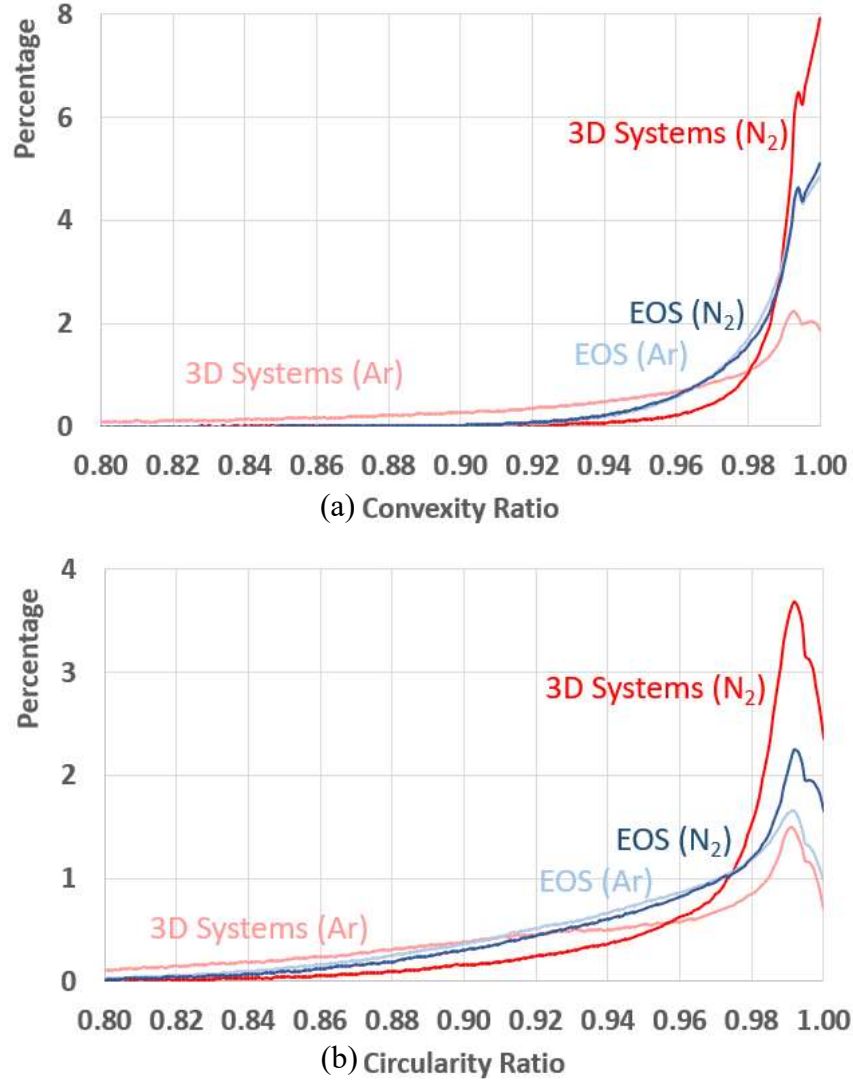


Figure 3.4: Image analysis results for the four powder feedstocks showing distributions of (a) convexity ratio and (b) circularity ratio

### 3.3 Powder Flow Characteristics

Particle size and morphology can influence the flowability of powders, as demonstrated by the rheological properties presented in Table 3.1. The 3D Systems nitrogen atomized powder showed the greatest resistance to flow, as evidenced the high angle of repose, Hausner ratio, and its relative Hall flow time. As the feedstock with the largest proportion of finer particles, the high surface area associated with these fine particles promotes cohesion through high surface energy and Van der Waals forces. [50] These fine particles allow more air to be entrapped



during packing, resulting in the considerably lower apparent density for the 3D Systems nitrogen atomized powder.

Select results from the tests performed on the REVOLUTION powder analyzer are shown in Table 3.2. Consistent with the results of the conventional test methods, the 3D Systems nitrogen atomized powder exhibited the greatest resistance to flow among the four powder feedstocks. In general, the slightly coarser powders for the EOS system demonstrated greater flowability than the finer powders acquired for the ProX 200, as noted by the lower break energies, avalanche energies, and packed avalanche angles. During the dynamic flow test, the avalanche angle measured for the argon atomized feedstock for the ProX 200 was lower than EOS argon atomized powder, but it maintained higher values in other categories. The coarser

Table 3.2: REVOLUTION powder analyzer dynamic flowability results

		3D Sys. ProX 200		EOS M280	
		Ar Atom.	N <sub>2</sub> Atom.	Ar Atom.	N <sub>2</sub> Atom.
<b>Dynamic Flow Test</b>	Flow Density (g/cm <sup>3</sup> )	3.507	3.151	3.322	3.791
	Avalanche Angle (deg.)	48.8°	54.9°	52.5°	46.2°
	Break Energy (kJ/kg)	75.5	74.9	58.2	68.7
	Avalanche Energy (kJ/kg)	39.1	45.3	33.2	31.2
	Surface Fractal	4.23	3.24	4.17	5.00
<b>Packed Test</b>	Packed Density (g/cm <sup>3</sup> )	3.706	3.102	3.357	4.192
	Volume Change	-4.1%	-2.2%	-3.6%	-3.0%
	Packed Avalanche Angle (deg.)	64.3°	54.8°	52.2°	48.7°
<b>Charge Test</b>	Max Charge, Glass(V)	80	412	58	66
	Max Charge, Polycarbonate (V)	429	910	333	-236

particles for the EOS System were also less likely to accumulate charge, whether in contact with a glass surface or polycarbonate surface as shown in Figure 3.5 (a) and (b), respectively.

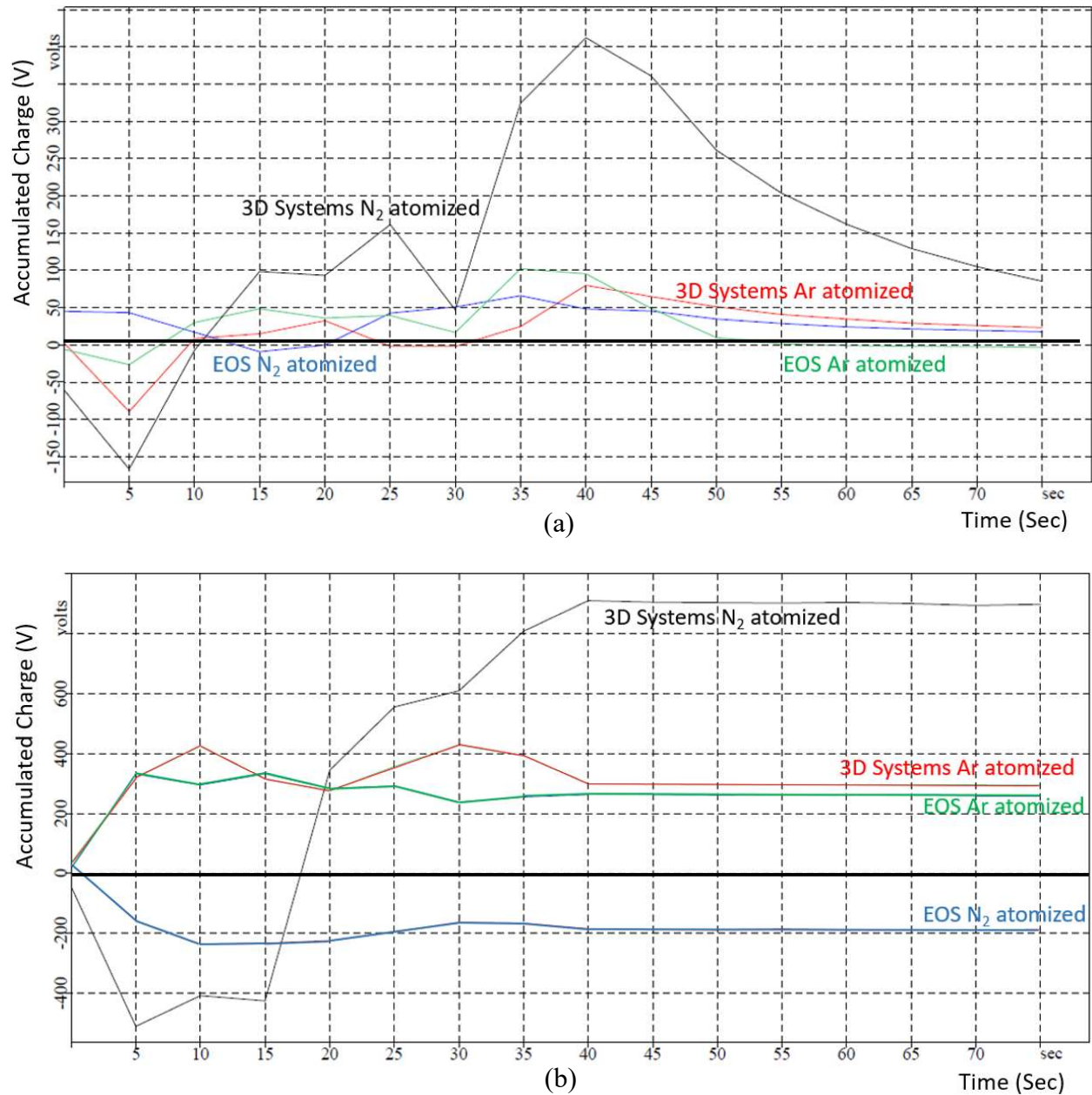


Figure 3.5: Accumulated charge versus time as measured by the REVOLUTION powder analyzer when powder is in contact with (a) glass or (b) polycarbonate

### 3.4 Chemical Composition of the Powder Feedstocks

The chemical compositions of the powder feedstocks are listed in Table 3.3. The obvious distinction is the higher nitrogen content within the nitrogen atomized feedstocks: 0.06 wt.% and 0.12 wt.% in the 3D Systems and EOS powders, respectively, compared to just 0.01 wt.% within either argon atomized powder. However, it is notable that that nitrogen atomized feedstocks also contained less Cr, slightly more Cu, and at least three times the C and Mn. These differences are important because, in addition to Ni, the elements Cu, Mn, C, and N are all known austenite stabilizers whereas Cr is a ferritic stabilizer [39].

The nickel and chromium equivalencies for the feedstocks (and subsequent builds), as calculated from equations (3) and (4) per the Balmforth constitution diagram [51], are also listed in Table 3.4. While the calculated  $Cr_{eq}$  values for all four feedstocks fall within the range of 16.6 to 17.7, the  $Ni_{eq}$  values of the nitrogen atomized feedstocks are significantly higher than the argon atomized material. The sharp contrast in  $Ni_{eq}$  consequently suppresses the calculated  $Cr_{eq}/Ni_{eq}$  ratios for the nitrogen atomized powders to a range of 1.9 to 2.8, versus 3.3 to 3.5 for the argon atomized powders. While higher  $Cr_{eq}/Ni_{eq}$  ratios are associated with the ferritic region of the Schaeffler diagram, lower  $Cr_{eq}/Ni_{eq}$  ratios predict that the solidification mode shifts closer to the austenitic region.

It should be noted that the  $Cr_{eq}$  values calculated for the powder feedstocks likely contain some error due to difficulties in accurately measuring Mo, which has a weight factor of 2 in the chromium equivalency calculation listed as equation (3). When measuring the very low concentrations of Mo in plants, the DCP-AES method was shown to produce results an order of magnitude higher than either ICP-AES or a more sensitive chemical method involving the catalysis of a KI-H<sub>2</sub>O<sub>2</sub>. [52] However, the opposite trend was observed in this study. The Mo concentration of the powder feedstocks assessed by ICP-AES was an order of magnitude higher than that observed in the fabricate components analyzed by DCP-AES. While qualitative comparisons remain of interest, the reported Mo values should be considered with caution.

### 3.5 XRD Analysis of the Powder Feedstocks

The volume fraction of austenite within the powders (as well as subsequent as-built and heat treated specimens) was determined by X-Ray Diffraction (XRD) using a PANalytical X'Pert Pro MPD with an Empyrean Cu anode operated at 45 kV and 40 mA, paired with a

Table 3.3: Chemical compositions of powder feedstocks and fabricated builds, with corresponding austenite volume fractions

		3D Systems ProX 200						EOS M280			
		Ar Atomized Feedstock			N <sub>2</sub> Atomized Feedstock			Ar Atomized Feedstock		N <sub>2</sub> Atomized Feedstock	
Specified Ranges (wt.%)		Praxair lot FE-276-3	As- Built (Ar)	As- Built (N <sub>2</sub> )	Phenix lot 14D1147	As- Built (Ar)	As- Built (N <sub>2</sub> )	LPW lot UK5032	As-Built (N <sub>2</sub> )	EOS lot F471301	As-Built (N <sub>2</sub> )
15.0 - 17.5	Cr	16.6	15.6	15.7	15.8	15.7	15.7	16.4	16.5	15.2	15.2
3.0 - 5.0	Ni	4.3	4.2	4.2	4.1	4.2	4.2	4.1	4.3	4.3	4.6
3.0 - 5.0	Cu	3.2	3.3	3.3	3.7	3.9	4.0	4.0	4.2	4.3	4.3
≤ 1.00	Si	0.81	0.70	0.68	0.80	0.66	0.66	0.43	0.38	0.72	0.67
≤ 1.00	Mn	0.19	0.14	0.17	0.61	0.54	0.51	0.19	0.15	0.68	0.57
0.15 - 0.45	Nb(+Ta)	0.20	0.22	0.23	0.24	0.24	0.23	0.29	0.25	0.26	0.25
≤ 0.07	C	0.01	0.005	0.010	0.03	0.04	0.03	0.02	0.017	0.06	0.058
≤ 0.040	P	0.013	0.010	0.010	0.017	0.019	0.019	0.016	0.019	0.008	0.018
≤ 0.030	S	0.006	0.004	0.004	0.004	0.002	0.003	0.002	0.002	0.004	0.005
—	Mo	0.13	0.012	0.020	0.92	0.098	0.100	0.06	0.009	0.89	0.098
—	N	0.01	0.010	0.017	0.06	0.088	0.091	0.01	0.027	0.12	0.142
—	O	0.06	0.052	0.085	0.09	0.084	0.098	0.04	0.036	0.02	0.031
%Austenite		< 1%	0%	0%	21%	9%	14%	3%	< 1%	97%	81%

Table 3.4: Ni equivalent and Cr equivalent weight fractions per Balmforth constitution diagram as calculated from chemical compositions for each feedstock and AM build, as well as volume fraction of retained austenite as measured by XRD

		Cr <sub>eq</sub>	Ni <sub>eq</sub>	Cr <sub>eq</sub> / Ni <sub>eq</sub> ratio	% Aust.
3D Systems ProX 200	<b>Ar. Atom. Feedstock</b>	<b>17.0</b>	<b>4.9</b>	<b>3.5</b>	<b>&lt; 1%</b>
	As-Built (Ar/Ar)	15.8	4.9	3.3	0%
	As-Built (Ar/N <sub>2</sub> )	15.6	4.6	3.4	0%
	<b>N<sub>2</sub> Atom. Feedstock</b>	<b>17.7</b>	<b>6.4</b>	<b>2.8</b>	<b>21%</b>
	As-Built (N <sub>2</sub> /Ar)	16.0	7.1	2.2	9%
	As-Built (N <sub>2</sub> /N <sub>2</sub> )	16.0	7.3	2.2	14%
EOS M280	<b>Ar Atom. Feedstock</b>	<b>16.6</b>	<b>5.0</b>	<b>3.3</b>	<b>3%</b>
	As-Built (Ar/N <sub>2</sub> )	16.6	5.5	3.0	< 1%
	<b>N<sub>2</sub> Atom. Feedstock</b>	<b>17.0</b>	<b>8.8</b>	<b>1.9</b>	<b>97%</b>
	As-Built (N <sub>2</sub> /N <sub>2</sub> )	15.4	9.4	1.6	81%

PIXcel 1D detector. The setup was comprised of a 0.020 mm Ni large  $\beta$  filter, 0.04 mm Soller slit, 10 mm beam mask, and a 2° antiscatter slit. The default scan covered a 2 $\theta$  range of 40°-100° using an automatic spot size of 10 mm, but if necessary, was reduced to 5 mm to accommodate smaller specimens. The software program MDI Jade 2010 (version 3.6.5) was used to identify and integrate peaks, from which the amount of retained austenite was calculated by the direct comparison method. [53,54]

Because a copper radiation source has sufficient energy to eject inner shell elections of iron atoms, the use of a monochromator is recommended to minimize the resulting fluorescence. [53,55] Figure 3.6 displays the large background that occurs when a monochromator is not used,

followed by the steps taken within the software to correct the diffraction pattern. First, the pattern observed using an automatic slit is transformed into the corresponding pattern for the conventional fixed slit. Then the background level is determined and established as the new

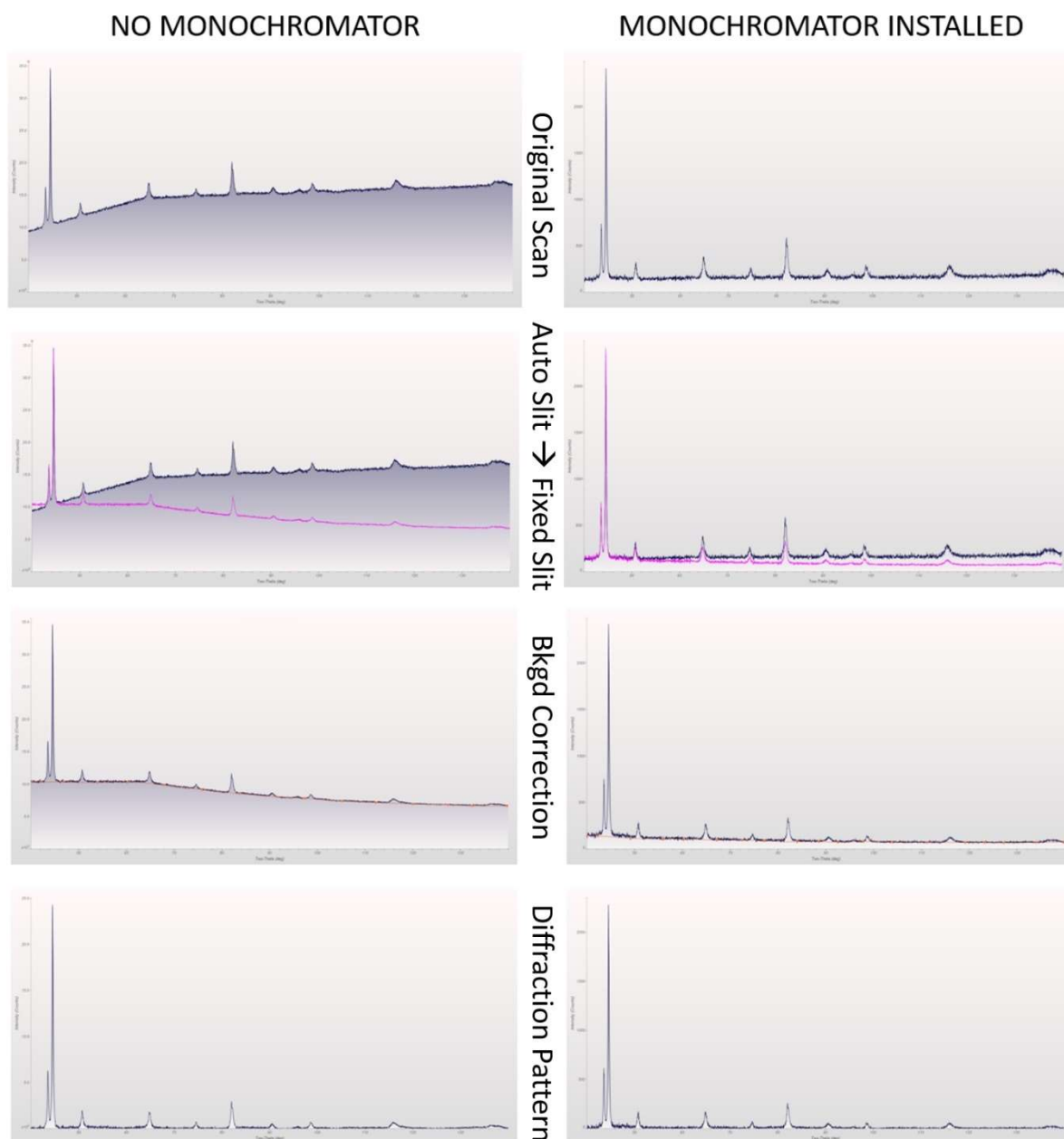


Figure 3.6: Comparison of XRD diffraction patterns of 3D Systems nitrogen atomized powder when scanned with or without a monochromator, both before and after software corrections

baseline. After these corrections, the resulting diffraction patterns with or without a monochromator were virtually indistinguishable on a normalized basis. Since the purpose of this study was limited to the direct comparison of the two primary phases and did not need to distinguish low intensity peaks, a monochromator was not used.

The most prominent peaks for each phase generally appeared at two-theta values of 43.6° and 44.5°, corresponding to FCC (111) and BCC (110), respectively. The precise position of these primary peaks was used in conjunction with Bragg's Law to determine the lattice spacing, followed by calculation of the lattice constant and unit cell volume. Table 3.5 lists the tabulated values [56] for multiplicity factor, atomic scattering factor, temperature factor, and the structure parameter  $R_i^{hkl}$  [53] for each hkl peak using the Cu K $\alpha$  source.

Table 3.5: Summary of parameters used to analyze x-ray diffraction data for determination of retained austenite volume fractions

			Atomic			Lorentz		calculated	
			Scattering	Structure	Multiplicity	Polarization	Temperature	proportional	
<i>h</i>	<i>k</i>	<i>l</i>	Factor, $f_{Fe}$	Factor, $F$	Factor, $p$	Factor, $LP$	Factor, $e^{-2M}$	parameter, $R_i$	
BCC Phase	1	1	0	17.5	2f	12	11.4	0.95	283.2
	2	0	0	14.8	2f	6	4.9	0.92	41.6
	2	1	1	13.0	2f	24	3.1	0.88	80.1
	2	2	0	11.8	2f	12	2.7	0.84	27.3
FCC Phase	1	1	1	17.6	4f	8	11.9	0.96	211.2
	2	0	0	16.5	4f	6	8.4	0.94	97.7
	2	2	0	13.7	4f	12	3.7	0.89	55.2
	3	1	1	12.3	4f	24	2.8	0.86	65.9
	2	2	2	11.9	4f	8	2.7	0.85	19.8

The austenite volume fraction could then be calculated by equation (5) [53]:

$$V_{\gamma} = \left( \frac{1}{q} \sum_{j=1}^q \frac{I_{\gamma j}}{R_{\gamma j}} \right) / \left[ \left( \frac{1}{P} \sum_{i=1}^P \frac{I_{\alpha i}}{R_{\alpha i}} \right) + \left( \frac{1}{q} \sum_{j=1}^q \frac{I_{\gamma j}}{R_{\gamma j}} \right) \right] \quad (5)$$

where the average ratio of integrated intensity to the proportional parameter,  $I/R$ , is calculated for the number of peaks being considered for the respective phases over the scanned two-theta range. The 40° to 100° range used in this study consists of four peaks for the BCC  $\alpha/\alpha'$  phase ( $P = 4$ ) and five peaks for the FCC  $\gamma$  phase ( $q = 5$ ). The low carbon content of  $\leq 700$  ppm specified for this alloy ensures that the lattice parameters of BCT martensite would remain quite similar to those of BCC ferrite [57], and therefore the two phases are considered to be identical in XRD analysis. The XRD patterns for the powders and as-built specimens are shown in Figure 3.7(a) and Figure 3.7(b), respectively.

The results of the XRD analysis listed in Table 3.3 demonstrate that the atomization condition had a significant impact on the austenite volume fractions. The argon atomized feedstocks with  $Ni_{eq} \leq 5$  retained only trace amounts of austenite. However, with higher concentrations of austenite stabilizing elements such as nitrogen, the nitrogen atomized feedstocks retained much larger austenite fractions. For example, 21% austenite was detected in the 3D Systems nitrogen atomized feedstock with a nitrogen concentration of 0.06 wt.% and a  $Ni_{eq}$  value of 6.4. The EOS nitrogen atomized material had the highest nitrogen concentration (0.12 wt.%) and  $Ni_{eq}$  value (8.8), and consequently was almost fully austenitic at 97%.

### 3.6 Summary and Conclusions

Morphology and flowability did not reveal any conclusive distinctions attributable to the choice of atomization gas. Rheological properties were most significantly impacted by particle size, with the finer feedstocks acquired for the 3D Systems ProX 200 generally exhibiting greater resistance to flow than the slightly coarser feedstocks for the EOS M280. Since each of the four powder feedstocks were acquired from different vendors, some of the dissimilarities could be attributed to variations in raw materials, processing equipment, or operating conditions. However, one clear distinction dictated by the atomization condition was the chemistry. Compared to just 0.01 wt.% nitrogen detected in either argon atomized feedstock, the nitrogen atomized powders acquired for the 3D Systems ProX 200 and EOS M280 contained nitrogen levels of 0.06% and 0.12%, respectively. These higher nitrogen concentrations, in



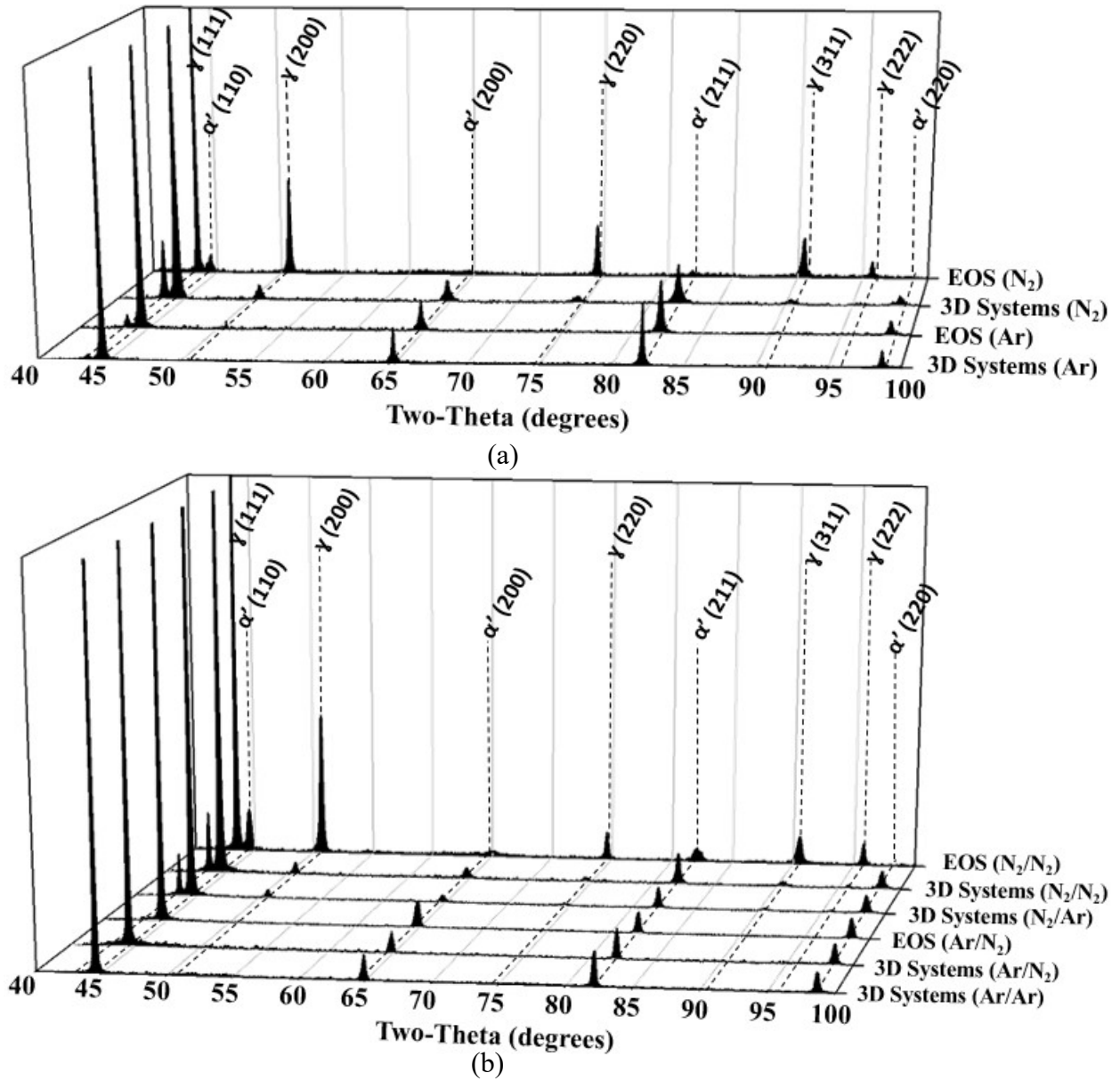


Figure 3.7: XRD patterns for AM 17-4 PH (a) feedstock and (b) in the as-built condition

addition to the contribution of other austenite-stabilizing elements like C and Mn, increased the nickel equivalency of the nitrogen atomized feedstocks. Since the variation in chromium equivalency was much narrower, the higher nickel equivalency values in the nitrogen atomized feedstocks suppressed the  $Cr_{eq}/Ni_{eq}$  ratios and drove the solidification mode closer to the austenitic region of the Schaeffler diagram. XRD analysis of the powders confirmed that while the argon atomized feedstocks were predominantly ferrite/martensite, the volume fraction of

austenite within the nitrogen atomized powders were measured as 21% and 97% for the 3D Systems ProX 200 and EOS M280 systems, respectively.

## Chapter 4

### ANALYSIS OF AS-BUILT MATERIAL

#### 4.1 Additive Manufacturing via Powder Bed Fusion

The argon and nitrogen atomized powder feedstocks procured for the EOS M280 and 3D Systems ProX 200 laser PBF systems were additively manufactured using the recommended operating parameters specific to each system. Separate builds were completed on the 3D Systems ProX 200 under either an argon or nitrogen atmosphere, while the two powder feedstocks for the EOS M280 were exclusively processed under nitrogen. Most of the builds consisted of 30 simple rectangular solids with a nominal cross-section of 63.5 mm  $\times$  6.35 mm, and build heights that ranged from 8.46 to 9.58 mm. However, due to limited feedstock, production from the argon atomized powder for the 3D Systems ProX 200 was limited to 10 bars under each atmosphere, with build heights of 7.70 mm when processed under nitrogen and 4.37 mm when processed under argon. Following fabrication, parts were removed from the base plate by electrical discharge machining. A cutting saw was then used to subdivide bars into 5-6 individual segments. Segments from each of the fabricated builds were sent to a certified testing laboratory<sup>8</sup> to determine the chemical composition through a combination of combustion infrared detection (C, S) and inert gas fusion (N, O) per ASTM E1019-11 [45], while the remaining elements were measured by direct current plasma atomic emission spectroscopy (DCP-AES) per ASTM E1097-12 [58].

#### 4.2 Chemical Composition of Fabricated Structures

The summarized chemistries presented in Table 3.3 show how the composition of the powder feedstocks correlate to the AM builds. Although some variability was introduced by altering the shielding gas, the processing atmosphere had only a minor impact on the composition. When the same feedstock was processed under either argon or nitrogen on the 3D Systems ProX 200, the as-built weight fraction of nitrogen differed by less than 0.01%. However, the greater disparities in nitrogen levels that were noted in the feedstocks were evident in the builds as well. While the components fabricated from argon atomized feedstocks contained 0.01 to 0.03wt.% nitrogen, the nitrogen atomized material yielded concentrations of around 0.09% for the 3D Systems material and exceeded 0.14% in the EOS powder. As

---

<sup>8</sup> Luvak Laboratories, Inc; Boylstown, MA

observed with the powders, the wide range of nitrogen concentrations leads to significant differences in the nickel equivalency, as revealed in Table 3.4.

Applying equations (3) and (4) to the specified composition ranges for 17-4 PH stainless steel [3] and plotting these ranges onto the Balmforth diagram [51], as shown in Figure 4.1, indicates that virtually all specified compositions of the alloy fall within the martensite+ferrite region. According to the diagram, only under the limited condition that  $Ni_{eq} > 7.08$  and  $Cr_{eq} > 16.86$  would any fraction of austenite be retained. However, since common standards do not specify a range for nitrogen [3,33], the calculated nickel equivalency for material that explicitly satisfies the compositional requirements could be much higher than the expected limit. For example, while the positions of the argon atomized materials processed on either system plotted in Figure 4.1 appear in the martensite+ferrite region of both the Balmforth[51] and Schaeffler[10] diagrams, the higher nickel equivalency of the 3D Systems nitrogen atomized material crosses into the austenite+martensite+ferrite region of the Schaeffler diagram. Although the nitrogen atomized material processed on the EOS system does not fall within the

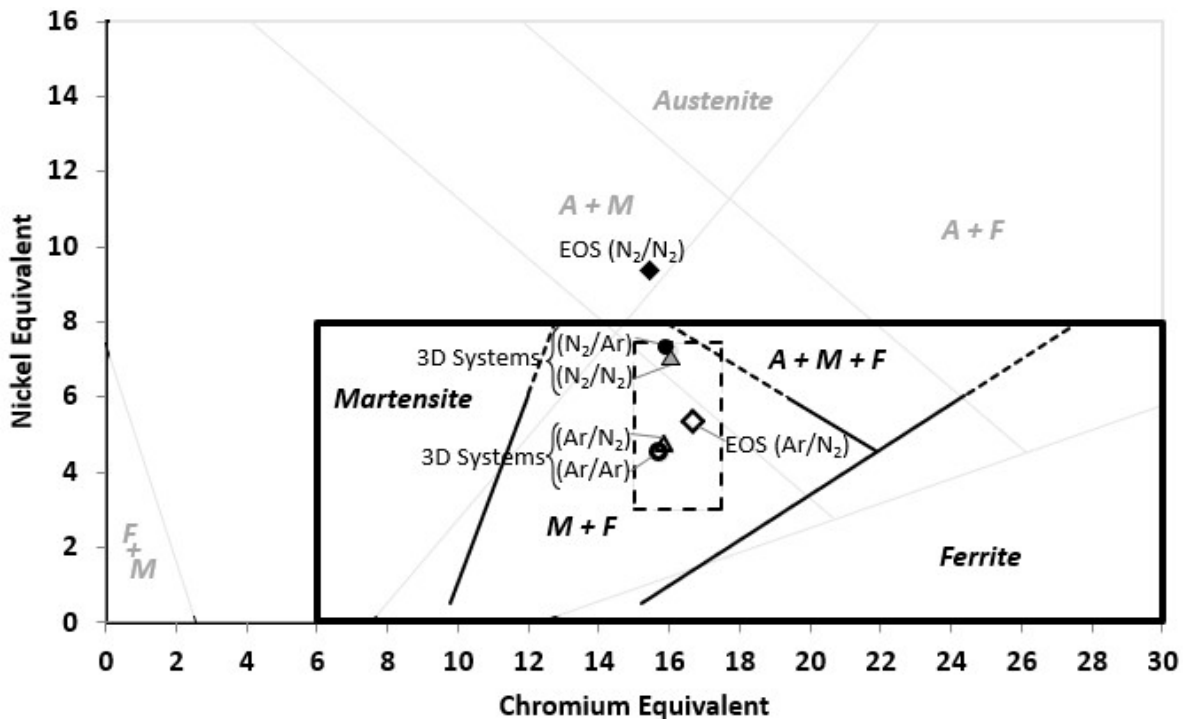


Figure 4.1: Balmforth diagram [51] showing the standard chemical composition [3] for 17-4 PH stainless steel (delineated by a dashed box), as well as the position of the six AM builds, overlaid on a subset of the Schaeffler diagram [10]

limits of the Balmforth diagram, when the same equivalency equations are applied, it appears in the austenite+martensite region of the Schaeffler diagram.

### **4.3 XRD Analysis of Fabricated Structures**

Comparing the chemistries in Table 3.3 with the XRD patterns in Figure 3.7(b) shows that the volume fraction of the austenite phase increased with higher levels of nitrogen. The XRD results listed at the bottom of Table 3.3 display trends that are consistent with the constitution diagram shown in Figure 4.1. The argon atomized materials in the martensite+ferrite region showed little to no retained austenite. The 3D Systems nitrogen atomized material, which bordered the austenite+martensite+ferrite region, was still primarily martensite+ferrite with only 9% or 14% retained austenite when processed under either argon or nitrogen atmospheres, respectively. Contrastingly, austenite was the predominant phase detected in the outlying EOS nitrogen atomized material. In all cases, the level of retained austenite measured in the AM components was lower than that of their respective powder feedstocks. Unlike the rapid solidification associated with gas atomization, which approaches an estimated cooling rate of  $10^7$  K/s for diameters smaller than 10  $\mu\text{m}$  [22], additively manufactured components undergo more complex thermal histories during which previously deposited layers experience some reheating that may affect solid state phase transformations [17]. Mechanical transformation to martensite induced by the metallographic preparation of the as-built surfaces has also been proposed as a contributing factor. [37]

### **4.4 Computational Modeling of Phase Equilibria**

The chemical composition of the fabricated components is primarily dictated by the feedstock chemistry, with only minor variations introduced by the selection of processing gas. The nickel and chromium equivalencies calculated from these chemical differences can influence the predicted phases that form within the alloy, as shown in Figure 4.1. An alternative method to predict the phase formation from the four powder feedstocks involved computing equilibrium mass fractions as a function of temperature according to each respective composition. Point calculations were used to capture the predicted solidification as well as solid state phase compositions to temperatures as low as 300°C.

The compositions of the four feedstocks were entered into JMatPro® software<sup>9</sup> to generate phase stability diagrams as a function of temperature using the CalPhaD thermodynamic approach. This computational approach was applied over temperatures ranging from about 300°C to above the liquidus temperature. To determine the relative proportions of ferrite and austenite phase upon solidification, Scheil calculations were used. The Scheil approach assumes that diffusion is infinitely fast within the liquid but does not occur within a solid once it is formed, and that equilibrium conditions exist at the solid-liquid interface.

Figure 4.2(a) and Figure 4.2(b) show the calculated phase compositions as a function of temperature based upon the chemistries of the argon atomized and nitrogen atomized feedstocks, respectively, processed on the 3D Systems ProX 200 system. Similar diagrams representing the compositions of both feedstocks for the EOS M280 system are shown in Figure 4.3(a) and Figure 4.3(b). The temperatures delineating phase boundaries are listed in Table 4.1, along with estimated volume fractions of austenite and ferrite predicted by Scheil solidification calculations.

Most of the feedstocks exhibit the FA solidification mode. After initially solidifying as ferrite, some austenite also begins to form, but ferrite remains the predominant phase. In contrast, the EOS nitrogen atomized feedstock represented in Figure 4.3(b) essentially exhibits fully austenitic (A) solidification.

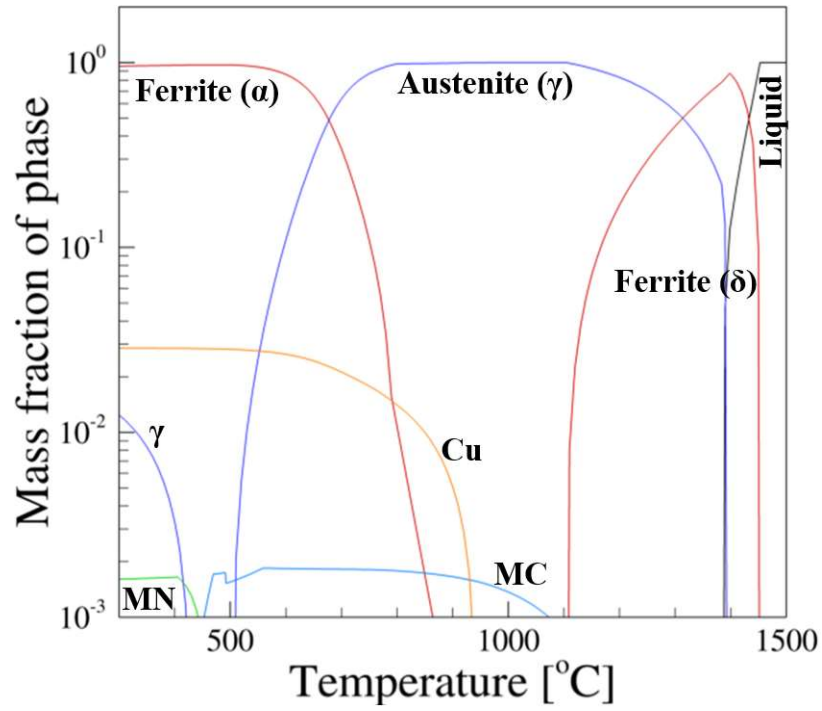
As the temperature progresses further below the solidus line, additional phases are predicted to form, including nitrides, various carbides, and a copper phase. The higher levels of carbon and nitrogen within the nitrogen atomized feedstocks for both systems corresponds to higher mass fractions of carbides and nitrides, though the net contribution from these minor phases remains relatively low.

#### **4.5 Estimation of Martensite Start Temperature**

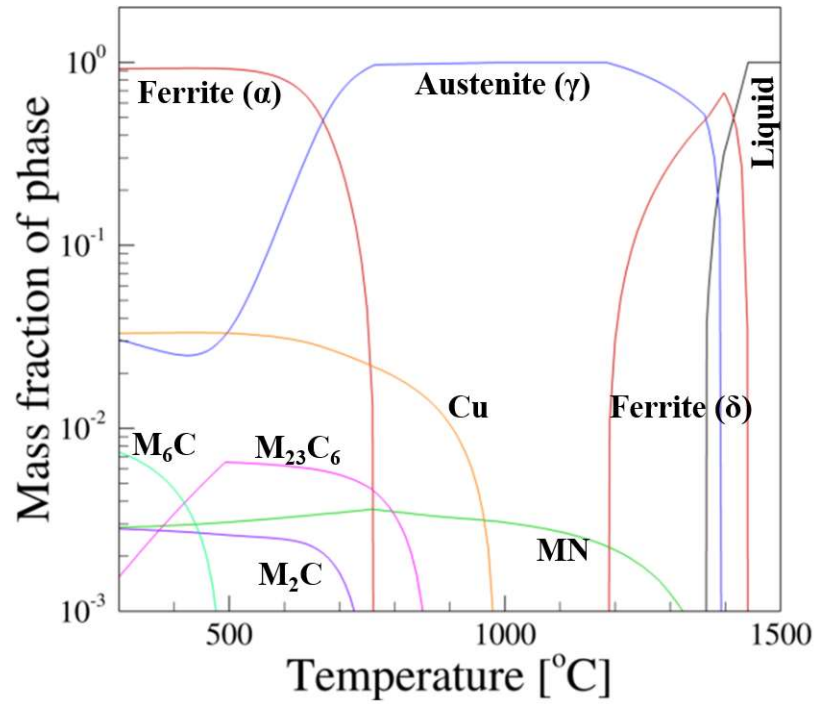
In addition to influencing the amount of austenite that forms during solidification, the chemical composition can also affect the extent of martensitic transformation. For example, higher concentrations of carbon [59,60] or manganese [61] within ferrous alloys have been shown to suppress the temperature at which martensitic transformation initiates. Lower

---

<sup>9</sup> Sente Software Ltd; Surrey, UK

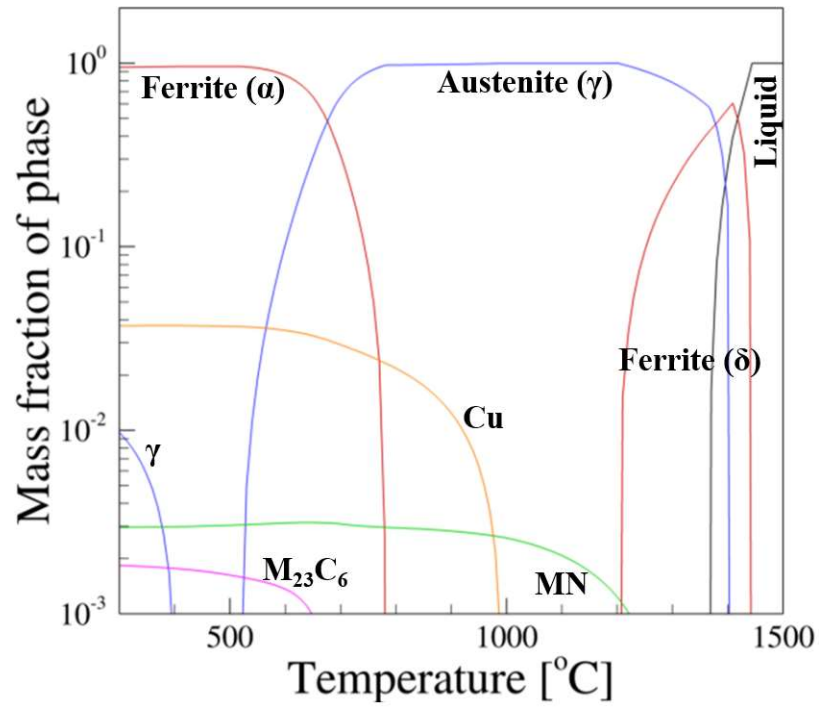


(a)

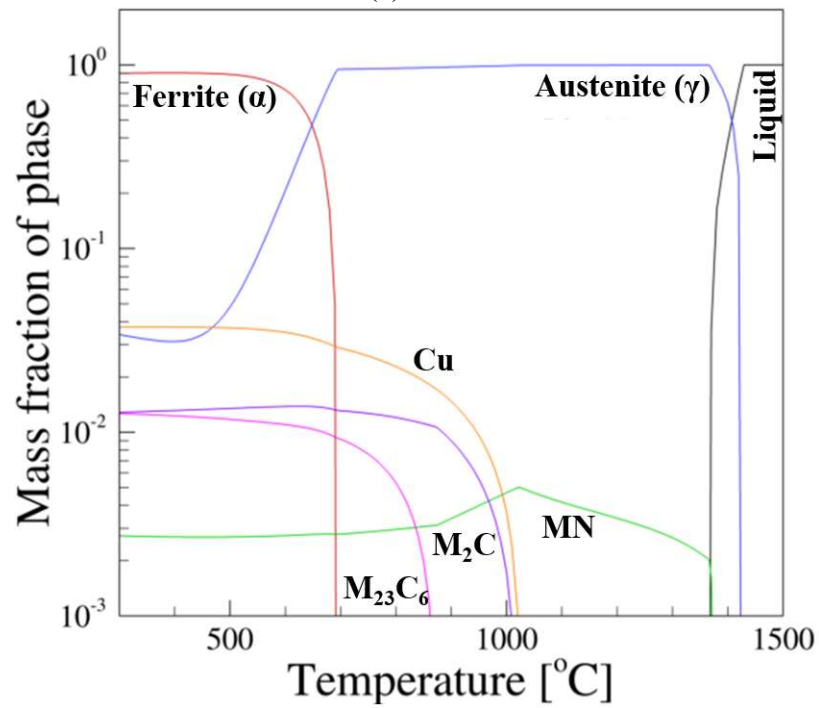


(b)

Figure 4.2: Equilibrium phase composition calculated as a function of temperature from the 3D Systems ProX 200 powder chemistries for (a) argon atomized and (b) nitrogen atomized feedstocks



(a)



(b)

Figure 4.3: Equilibrium phase composition calculated as a function of temperature from the EOS M280 powder chemistries for (a) argon atomized and (b) nitrogen atomized feedstocks



Table 4.1: Summary of phase equilibrium temperatures and Scheil solidification calculations computed from the chemical compositions of the four powder feedstocks

	3D Systems ProX 200		EOS M280	
	Ar atomized	N <sub>2</sub> atomized	Ar atomized	N <sub>2</sub> atomized
<b><u>Equilibrium calculations</u></b>				
Liquidus Temp. (°C)	1453	1441	1444	1429
Solidus Temp. (°C)	1384	1362	1367	1367
Austenite region(s) (°C)	1399 – 501, Below 431	Below 1398	1409 – 519, Below 405	Below 1429
Ferrite region(s) (°C)	1453 – 1104, Below 800	1441 – 1184, Below 765	1444 – 1202, Below 781	Below 695
Cu phase formation Temp. (°C)	944	986	994	1027
<b><u>Scheil Solidification calculations</u></b>				
Solidification range (°C)	1453 to 1225	1441 to 1225	1444 to 1230	1429 to 1245
Volume fractions (Ferrite/Austenite)	0.80/0.19	0.67/0.32	0.64/0.35	0.004/0.99

martensite start ( $M_s$ ) temperatures reduce the likelihood of the transformation nearing completion at room temperature, corresponding to higher levels of retained austenite.

The  $M_s$  temperature was estimated as a function of nitrogen composition for each of the fabricated conditions. A thermodynamic approach was used to identify the temperature at which the difference in Gibbs free energy of the austenite and ferrite phases was sufficiently large enough to initiate nucleation of martensite. [62] Calculations were based exclusively on the composition of the austenite within each build, after accounting for some consumption of solute into secondary phases. Grain size of the austenite, however, was not taken into account.

Figure 4.4 reveals how the chemical compositions within the builds affect the  $M_s$  temperature, and specifically highlights the significant role of nitrogen. Among the six builds,

the highest projected  $M_s$  temperature (223°C) corresponded to the argon atomized feedstock for the 3D Systems ProX 200, which possessed the lowest levels of austenite-stabilizing elements C, N, Mn, and Cu. Conversely, the austenitic material with the highest nickel equivalency was projected to be 99° lower at 124.65°C, of which approximately 56°C can be attributed to the difference in nitrogen alone.

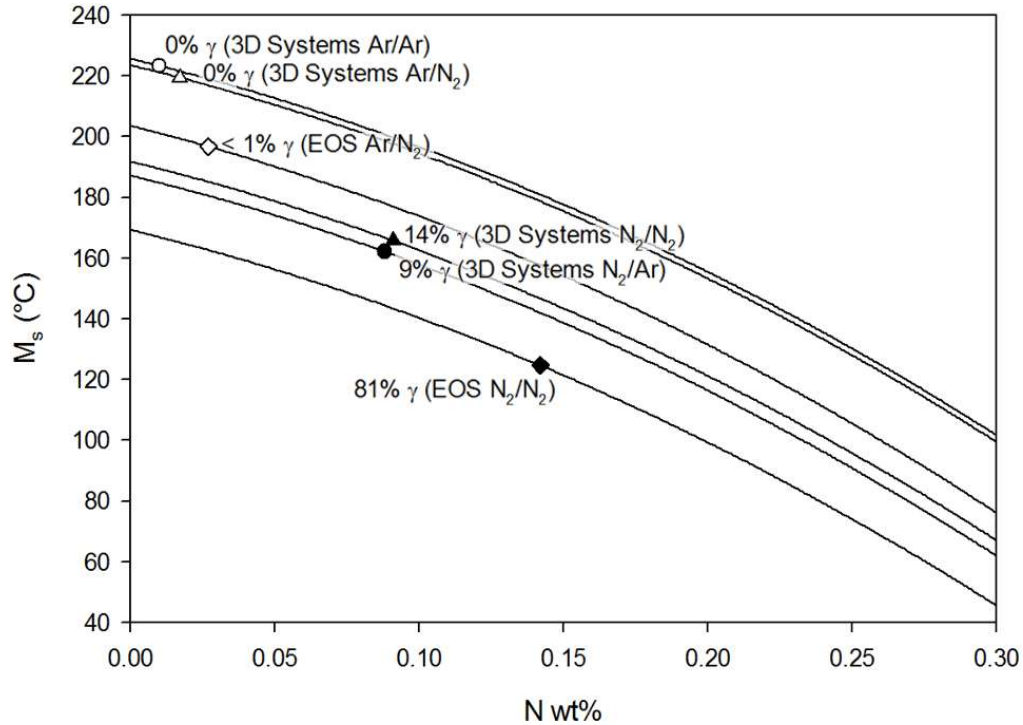


Figure 4.4: Simulated martensite start temperature as a function of nitrogen weight percent for each build composition

#### 4.6 Metallographic Analysis of Fabricated Structures

In preparation for further characterization, specimens representing each of the different conditions were individually mounted in an epoxy thermosetting powder using a Struers ProntoPress-2 operated at approximately 30 kN and 185°C. After grinding the surface of the specimens through a series of silicon carbide sheets to a rating of 1200 (FEPA P4000) microgrit on a Struers Pedemax-2, the samples were polished with a 3  $\mu$ m diamond suspension and 1  $\mu$ m diamond suspension for 2 minutes each. A final polishing step with a 0.06  $\mu$ m colloidal silica suspension was performed for 8 minutes. To assess the hardening response throughout the heat

treatments, a minimum of 30 Vickers microhardness measurements per specimen were recorded with a Leco M-400-G1 Hardness Tester set to a load of 300 g<sub>F</sub>. Specified hardness ranges for wrought 17-4 PH stainless steel are presented on the Rockwell C scale, so to allow for comparisons, a standard conversion table for non-austenitic steels [63] was used to determine the corresponding Vickers hardness numbers.

Select specimens were immersed for 6-11 seconds in a solution of Marble's etchant (50 ml HCl + 50 ml H<sub>2</sub>O + 10 g CuSO<sub>4</sub>) [64] diluted 50/50 with glycerol. Optical micrographs were then captured using a Nikon Epithot microscope connected to a Digital Sight DS-Fi2 camera and Digital Sight DS-U3 camera controller. Following 12 hours of vibratory polishing, an FEI Helios NanoLab 660 scanning electron microscope equipped with an X-Max<sup>N</sup> detector (Model 51-XXM1005) was used in conjunction with Oxford Instruments Aztec 3.1 SP1 software to acquire energy-dispersive x-ray spectroscopy (EDS) maps.

Though intermediate iso-ferrite lines were not displayed in Figure 4.1, the positions of all three builds fabricated from the argon atomized powders fell within a range of 40% to 50% ferrite volume fraction [51]. Correspondingly, as shown in Figure 4.5(a) through (c), the three argon atomized builds also shared similar microstructures, consisting of long columnar laths that extended parallel to the build direction across several build layers. The predominantly austenitic structure shown in Figure 4.5(f) showed far less contrast, while the 3D Systems nitrogen atomized builds shown in Figure 4.5(d) and (e), which fall within the A+M+F region of the Schaeffler diagram in Figure 4.1, exhibited a complex microstructure that obscured the visibility of the semi-elliptical melt pools. EDS maps generated from each of the builds fabricated on the EOS M280 system did not reveal any distinct elemental segregation, as shown in Figure 4.6(a) and (b).

Hardness measurements of the as-built material will be presented in greater detail in Chapter 5, where they serve as a baseline to assess the impact of post-processing heat treatments. The three argon atomized builds, which had a consistent microstructure containing little to no retained austenite, all had a hardness of approximately 300 HVN. In contrast, the nitrogen atomized material produced on the EOS M280 that was primarily comprised of the softer austenitic phase had lower hardness (260 HVN). Although the 3D Systems nitrogen atomized builds also retained some austenite (9% and 14%), their placement on the constitution diagram

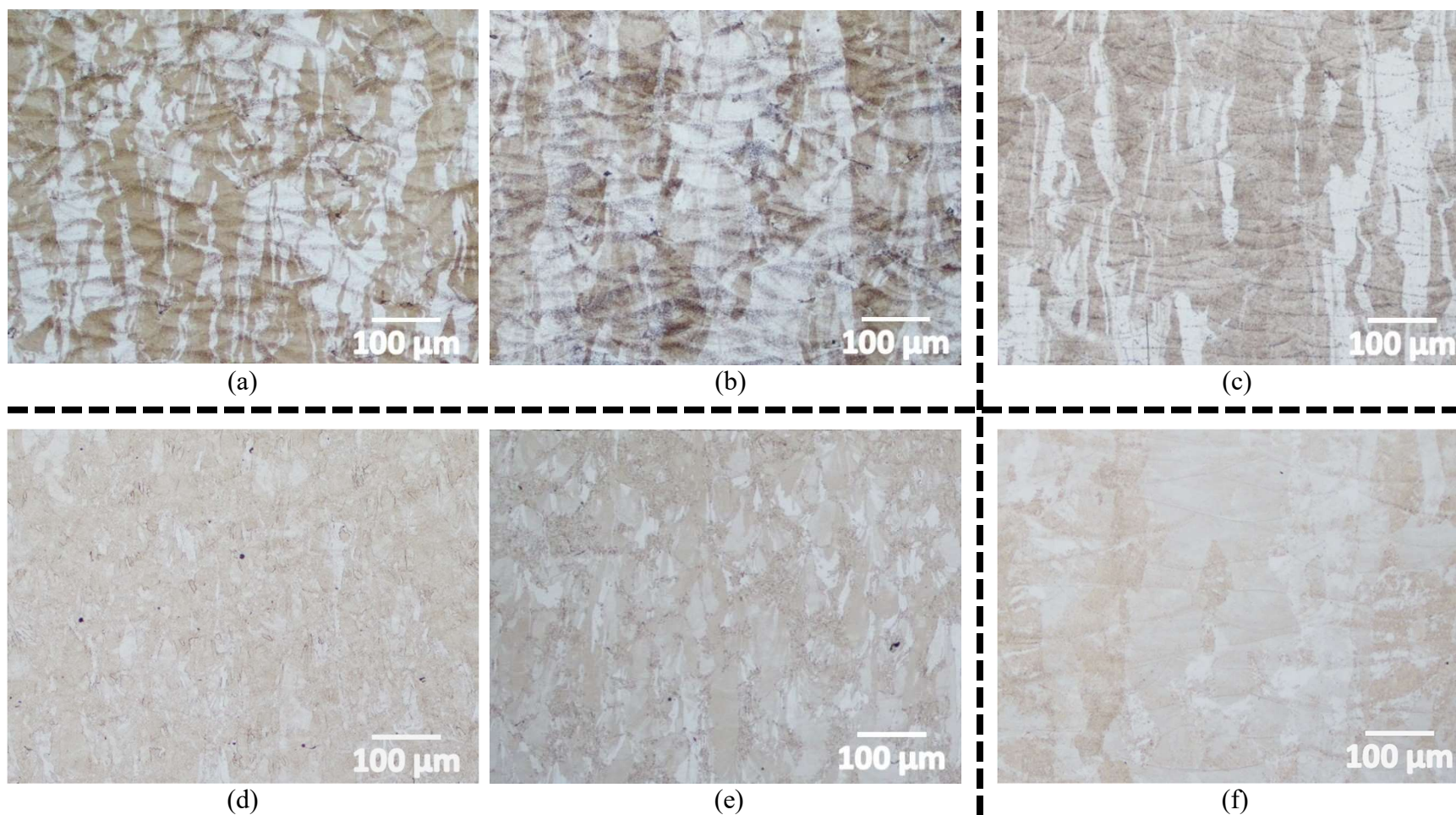


Figure 4.5: As-Built microstructures from (a) argon atomized feedstock for the 3D Systems ProX 200 processed under Ar atmosphere or (b) N<sub>2</sub> atmosphere; (c) argon atomized feedstock for EOS M280 (N<sub>2</sub> atmosphere); (d) nitrogen atomized feedstock for the ProX 200 processed under Ar atmosphere or (e) N<sub>2</sub> atmosphere; (f) nitrogen atomized feedstock for EOS M280 (N<sub>2</sub> atmosphere)

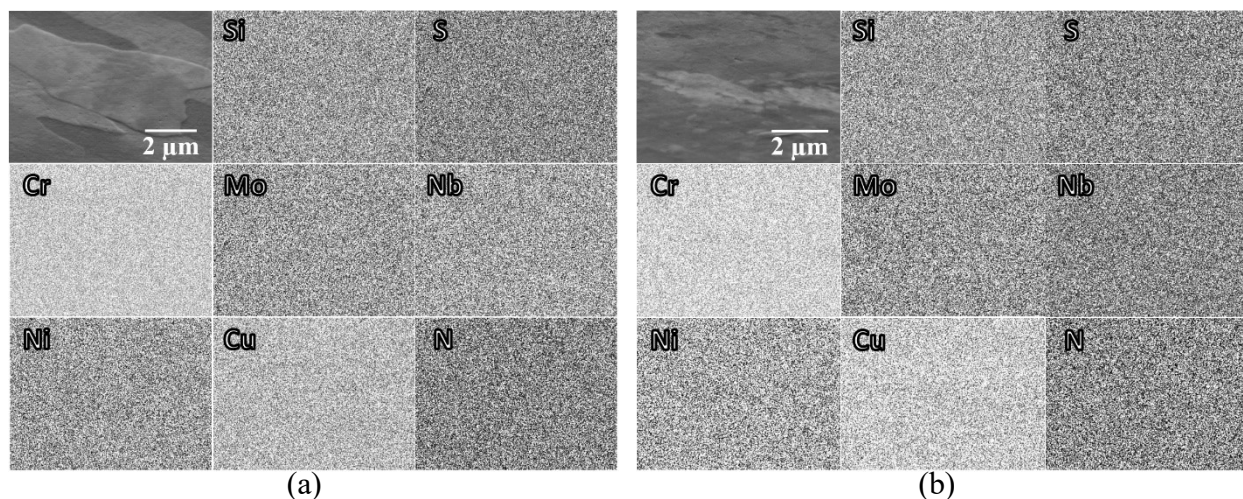


Figure 4.6: EDS maps showing no observable elemental segregation for builds fabricated on the EOS M280 system from (a) argon atomized powder or (b) nitrogen atomized powder

shown in Figure 4.1 predicts a lower ferrite content than any of the argon atomized products, thus allowing for more of the harder martensitic phase. Furthermore, the hardness of the martensite phase itself increases with higher concentrations of the solute. [65] Even though the nitrogen atomized feedstocks for both systems possessed greater levels of carbon and nitrogen compared to either argon atomized material, only the 3D Systems builds had a mostly martensitic structure, and consequently, had the highest hardness in the as-built condition (~340 HVN). For both feedstocks processed on the 3D Systems ProX 200, the minor increase in nitrogen content associated with changing the processing atmosphere from argon to nitrogen also resulted in a slight increase in hardness.

#### 4.7 Summary and Conclusions

The chemical composition of the AM components is primarily dictated by the powder feedstocks, with only minor variations introduced by the choice of shielding gas. For chemistries that coincide with the nickel and chromium equivalencies calculated for specified elemental ranges of the 17-4 PH alloy, thermodynamic calculations predict an initial solidification into ferrite, and maintaining a predominantly BCC structure. However, differences in nitrogen—a non-specified element—can sufficiently alter the  $Cr_{eq}/Ni_{eq}$  ratios into an austenitic solidification mode. Higher concentrations of austenite stabilizing elements also suppress the martensite start ( $M_s$ ) temperature of the alloy, potentially leading to higher levels of retained austenite. Hardness

values ranging from 260 to nearly 350 HVN could be attributed to the different proportions of the phases present, and ultimately, the chemistry.

### 5.1 Overview of Post-Fabrication Heat Treatments

To assess the heat treatment response of the six AM builds, selected segments were subjected to various heat treatment conditions. A Rapid Temp Furnace<sup>10</sup> was preheated to the target temperature under a constant flow of argon, and then samples were placed inside. At the end of the designated duration, samples were removed and permitted to air-cool to room temperature. Although various standards specify a temperature range for the solutionizing heat treatment, including  $1040\pm 15^{\circ}\text{C}$  [33],  $1052\pm 27^{\circ}\text{C}$  [3], or  $1038\pm 14^{\circ}\text{C}$  [44], only the latter specifies a duration ( $\geq 30$  minutes). Therefore, soak durations of 15, 30, 60, or 90 minutes were all tested at the solutionizing temperature of  $1040^{\circ}\text{C}$ . Four hour overaging heat treatments were conducted at temperatures of  $495^{\circ}\text{C}$ ,  $580^{\circ}\text{C}$ , and  $1150^{\circ}\text{C}$ , in accordance with the standard H925, H1075, and H1150 heat treatments [3,33], respectively.

As depicted in Figure 5.1, aging heat treatments followed four possible heat treatment paths, including aging directly from the as-built condition, as part of a two-stage heat treatment following an initial 30 minute solutionizing step, and finally within three-stage processes that incorporated an initial homogenization step of 90 minutes at  $1149\pm 14^{\circ}\text{C}$  [44]. While one version of the three-stage process maintained the practice of allowing specimens to air-cool following solutionization, alternate specimens were water-quenched at this step. In the case where the standard overaged response was not observed, additional multi-stage heat treatments were conducted at aging temperatures of  $550^{\circ}\text{C}$ ,  $650^{\circ}\text{C}$ ,  $680^{\circ}\text{C}$ ,  $720^{\circ}\text{C}$ , and  $760^{\circ}\text{C}$ , after solutionizing for either 30 or 60 minutes.

### 5.2 Direct-Aging Heat Treatment

The differences in the as-built condition discussed in Chapter 4 can be expected to produce variations in the heat treatment response. The first series of heat treatments conducted for this study involved aging all of the materials for four hours directly from the as-built condition at temperatures of  $495^{\circ}\text{C}$ ,  $580^{\circ}\text{C}$ , or  $620^{\circ}\text{C}$ . The resulting hardness values and retained austenite fractions are listed in Table 5.1. The progression of the hardness values is then

---

<sup>10</sup> CM Furnaces, Inc; Bloomfield, NJ



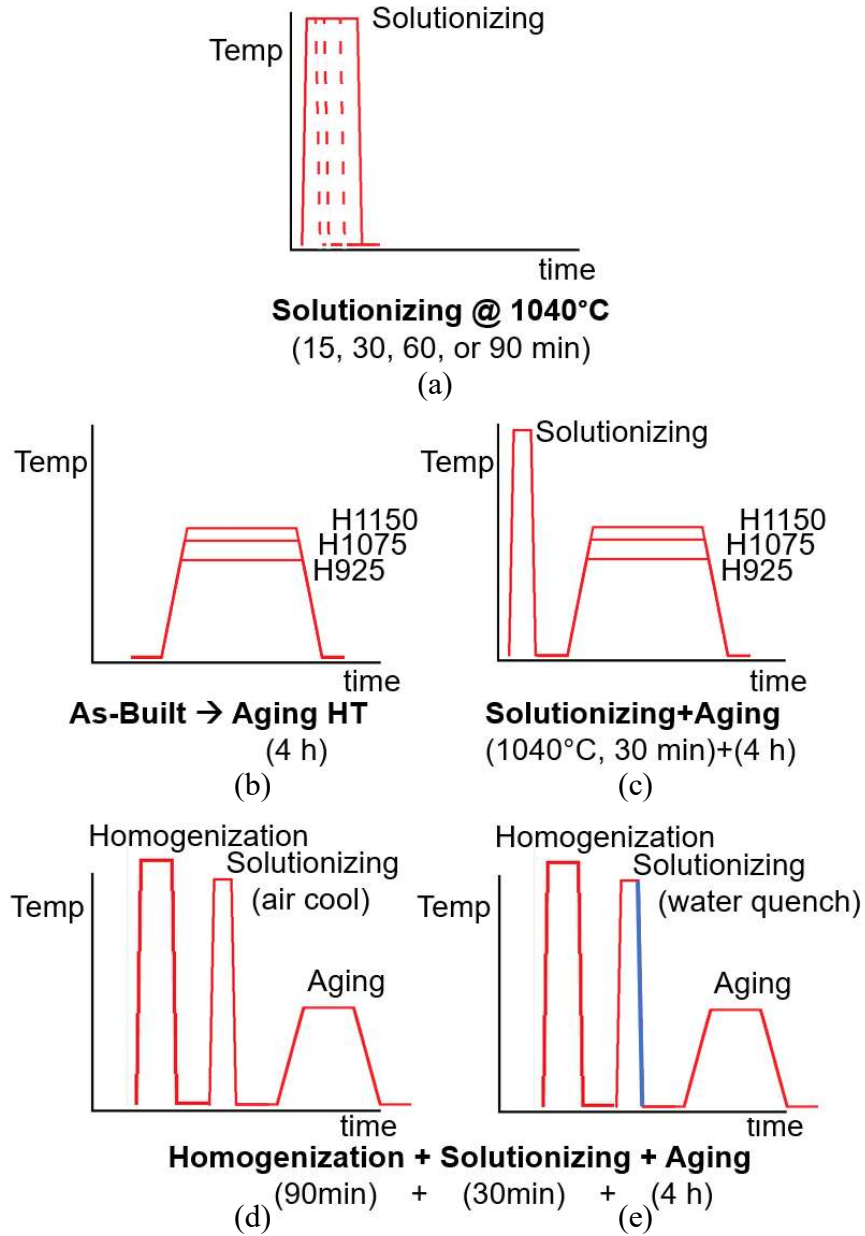


Figure 5.1: Schematic of various heat treatment cycles, including (a) solutionizing for different durations, (b) aging directly from the as-built condition, (c) a two-stage heat treatment, and three-stage processes for which post-solution specimens were either (d) air-cooled or (e) water-quenched

visually depicted in Figure 5.2(a) and (b) for the 3D Systems ProX 200 and EOS M280, respectively, with specified limits for each condition [3] indicated by brackets. A dashed line is used to represent the maximum hardness specified for the solutionized state of wrought 17-4 PH



Table 5.1: Comparison of austenite volume fraction and Vickers microhardness after 4-hour aging directly from the as-built condition

		Ar/Ar		Ar/N <sub>2</sub>		N <sub>2</sub> /Ar		N <sub>2</sub> /N <sub>2</sub>		
		% $\gamma$	HVN	% $\gamma$	HVN	% $\gamma$	HVN	% $\gamma$	HVN	
3D Sys. ProX 200	Feedstock	<1%	—	<1%	—	21%	—	21%	—	
	As-Built	0%	299±12	0%	312±8	9%	339±10	14%	348±8	
	Aging HT	495°C	0%	382±9	0%	402±12	22%	404±18	15%	422±10
		580°C	1%	275±9	<1%	291±7	19%	329±9	20%	338±7
		620°C	<1%	257±6	<1%	270±4	18%	353±17	18%	349±10

EOS M280	Feedstock		3%	—		97%	—	
	As-Built		<1%	298±7		81%	260±7	
	Aging HT	495°C		<1%	384±9		87%	256±7
		580°C		1%	290±6		48%	279±10
		620°C		2%	279±5		40%	367±22

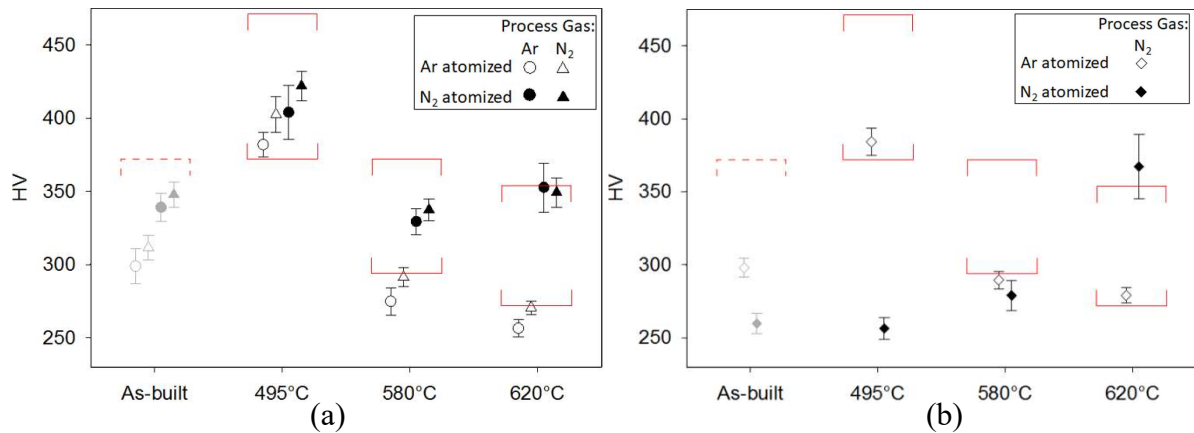


Figure 5.2: Vickers hardness measurements compared to specification range for standard wrought materials when aged for 4 hours directly from the as-built condition for (a) 3D Systems ProX 200 and (b) EOS M280 system

grade [3], known as “Condition A.” Because the additively manufactured components generally satisfy this hardness requirement, the as-built condition has previously been considered equivalent to the solutionized state [36,66].

Although material fabricated from either of the argon atomized feedstocks met the specification for the heat treatment closest to the peak age condition, the hardness of materials overaged at higher temperatures often fell below the minimum. Among the 3D Systems builds, the higher hardness observed in the as-built condition of nitrogen atomized materials was evident in the aged conditions as well, allowing both nitrogen atomized builds on the ProX 200 to generally satisfy hardness requirements. However, contradictory to the expected decline associated with overaging, hardness values for the 3D Systems nitrogen atomized materials actually increased following aging at 620°C compared to 580°C. The deviation from the expected overage response was even more pronounced in the highly austenitic material processed on the EOS M280 system. Consistent with a previous study[34] that applied the standard H900 peak-aging heat treatment (1 h at 482°C [3]) to AM 17-4 PH grade with a mostly austenitic structure, aging at 495°C showed little change from the as-built condition. Hardness values then proceeded to increase with increasing aging temperature.

The increasing hardness of the EOS nitrogen atomized material coincides with a reduction in the retained austenite fraction, as it transitions from a primarily austenitic structure at the low overaging temperature to a mostly martensitic one at higher temperatures. Each of the other builds, however, showed a slight increase in the austenite volume fraction upon aging, indicating that reverted austenite was generated. This is attributed to the diffusion of austenite-stabilizing elements such as Cu and Ni into localized regions, thereby lowering the martensite start temperature. [2,37,67]

### **5.3 Two-stage Heat Treatment: Solutionizing Followed By Aging**

The prior section showed that when samples were aged directly from the as-built condition, austenite levels within the AM components heavily influenced the heat treatment response. Subjecting AM components to a solutionizing heat treatment prior to aging, however, should lessen variations in the as-built microstructure. [41] However, since the soak duration at the solutionizing temperature is generally not specified [3,33], different soak times ranging from 15 to 90 minutes were tested.

The results in Table 5.2 and the corresponding hardness plots in Figure 5.3 show that the majority of the builds exhibited little sensitivity to solutionizing duration, with the exception of the highly austenitic material. Therefore, the recommended minimum duration of 30 minutes [44] was selected as the default solutionizing time for subsequent heat treatments.

For the builds fabricated on the 3D Systems ProX 200, Figure 5.3(a) reveals that the nitrogen atomized material exhibited a greater increase in hardness from the as-built condition than the argon atomized material, corresponding to a reduction in the volume fraction of the softer austenite phase. Although the nitrogen atomized material for the EOS M280 also showed a significant reduction in retained austenite, the  $\gamma$ -phase volume fraction remained above 20%. Among the builds dominated by the  $\alpha/\alpha'$  phase following solutionizing ( $\leq 4\% \gamma$ ), hardness values in the solutionized condition were higher for increasing levels of nitrogen (Table 3.3).

After subjecting each of the specimens to a 30 minute solutionization at 1040°C, the overaging heat treatments discussed in Section 5.2 were once again applied. Hardness measurements and austenite fractions following the two-stage heat treatments are presented in Table 5.3. When compared to the specified hardness ranges for each condition [3], Figure 5.4 shows that the inclusion of the solutionization step improved the aging response. Though the argon atomized material processed on either system failed to consistently achieve sufficient hardness levels when aged directly from the as-built condition, the results following a two-stage heat treatment generally satisfied the wrought specifications. Furthermore, the nitrogen atomized material fabricated on the 3D Systems ProX 200 now exhibited the expected overage response of declining hardness values for increased aging temperatures. While the austenite fraction of the EOS nitrogen atomized material did not substantively change upon aging, the material with intermediate nitrogen levels ranging from 0.088 to 0.091 wt.% (per Table 3.3) exhibited increasing levels of reverted austenite with higher nitrogen content. Although less reverted austenite was observed in the argon atomized material, an example of the elemental segregation of nickel and chromium following overaging at the higher temperature is visible in Figure 5.5. Similar to the direct-aging results in Figure 5.2(b), Figure 5.4(b) shows that the material fabricated from the highly austenitic nitrogen atomized feedstock continued to increase in hardness at higher aging temperatures, indicative of an underaged condition.

Table 5.2: Comparison of austenite volume fraction and Vickers microhardness after solutionizing at 1040°C for different durations

		Ar/Ar		Ar/N <sub>2</sub>		N <sub>2</sub> /Ar		N <sub>2</sub> /N <sub>2</sub>		
		% $\gamma$	HVN	% $\gamma$	HVN	% $\gamma$	HVN	% $\gamma$	HVN	
3D Systems ProX 200	Feedstock	<1%	—	<1%	—	21%	—	21%	—	
	As-Built	0%	299±12	0%	312±8	9%	339±10	14%	348±8	
	Solution HT	15 min	<1%	303±11	<1%	315±6	5%	368±15	4%	374±9
		30 min	0%	302±15	0%	315±11	4%	351±12	4%	368±13
		60 min	0%	301±9	0%	309±10	3%	355±13	1%	371±27
		90 min	0%	298±10	0%	306±6	2%	351±22	1%	366±16

EOS M280	Feedstock		3%	—		97%	—	
	As-Built		<1%	298±7		81%	260±7	
	Solution HT	15 min		0%	325±4		28%	273±25
		30 min		0%	321±5		24%	262±22
		60 min		0%	321±5		22%	356±10
		90 min		<1%	319±5		25%	321±24

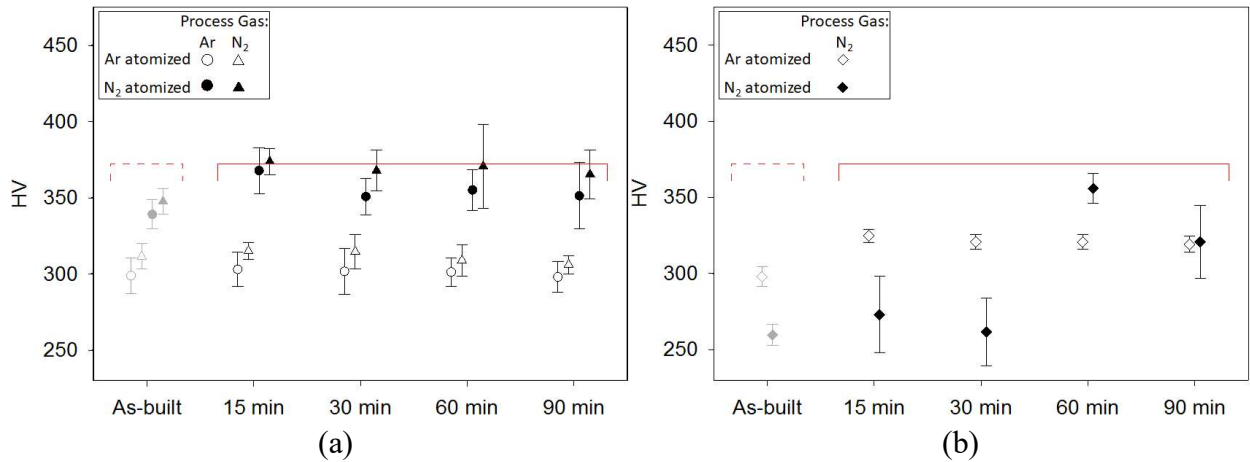


Figure 5.3: Vickers hardness measurements following solutionizing at 1040°C for different durations, as compared to specified maximum for standard wrought materials, for (a) 3D Systems ProX 200 and (b) EOS M280 system

Table 5.3: Comparison of austenite volume fraction and Vickers microhardness after 30-min solutionizing heat treatment at 1040°C followed by 4-hour aging; fabricated on 3D Systems ProX 200

		Ar/Ar		Ar/N <sub>2</sub>		N <sub>2</sub> /Ar		N <sub>2</sub> /N <sub>2</sub>	
		% $\gamma$	HVN	% $\gamma$	HVN	% $\gamma$	HVN	% $\gamma$	HVN
3D Sys. ProX	Post-Soln	0%	302 $\pm$ 15	0%	315 $\pm$ 11	4%	351 $\pm$ 12	4%	368 $\pm$ 13
	495°C	<1%	372 $\pm$ 6	5%	373 $\pm$ 5	4%	393 $\pm$ 9	7%	379 $\pm$ 6
	580°C	0%	315 $\pm$ 6	6%	319 $\pm$ 7	16%	355 $\pm$ 5	22%	346 $\pm$ 7
	620°C	0%	290 $\pm$ 7	<1%	299 $\pm$ 4	30%	309 $\pm$ 6	22%	340 $\pm$ 15
EOS M280	Post-Soln			0%	321 $\pm$ 5			24%	262 $\pm$ 22
	495°C			<1%	396 $\pm$ 4			22%	273 $\pm$ 23
	580°C			9%	328 $\pm$ 6			24%	391 $\pm$ 10
	620°C			5%	300 $\pm$ 4			20%	414 $\pm$ 11

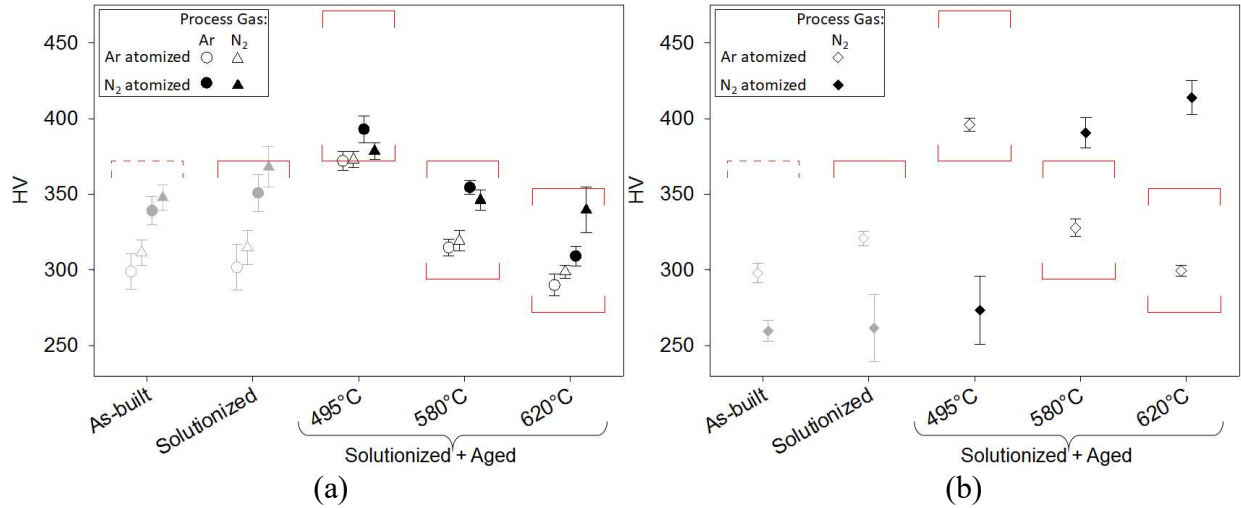


Figure 5.4: Vickers hardness measurements compared to specification range for standard wrought materials following two-stage heat treatment consisting of 30-min solutionizing followed by 4-hour aging for (a) 3D Systems ProX 200 and (b) EOS M280 system

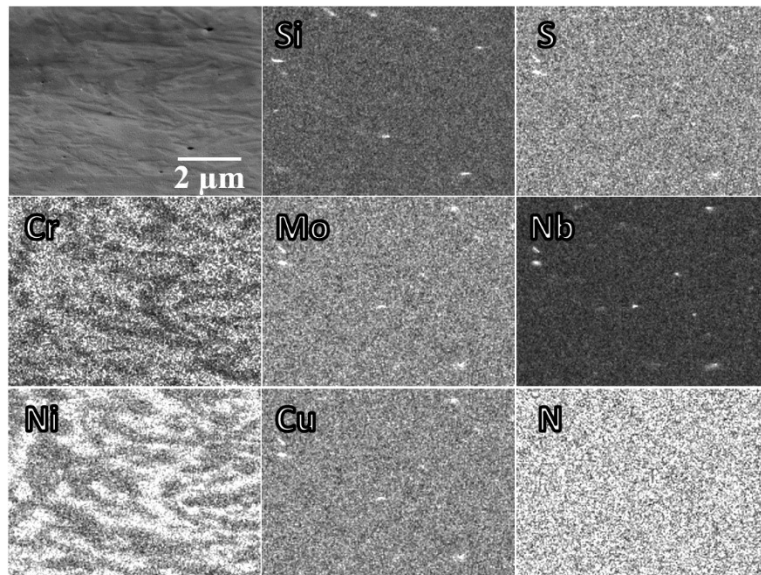


Figure 5.5: Elemental segregation of chromium and nickel observed in argon atomized material processed on the EOS M280, after solutionizing followed by aging at 620°C

#### 5.4 Determination of Peak-Aging for Highly Austenitic Material

Because the material fabricated from the highly austenitic feedstock had not yet demonstrated an overage response, additional two-stage heat treatments were conducted at aging temperatures up to 760°C. Also, since this material showed a sensitivity to solutionizing duration (Figure 5.3), the series of four-hour aging heat treatments was repeated for material solutionized at 1040°C for 60 minutes. As revealed in Table 5.4 and graphically depicted in Figure 5.6, hardness values proceeded to level off at aging temperatures above 620°C before finally demonstrating an overage response at temperatures in excess of 700°C. The maximum observed hardness, following four-hour aging at 680°C, satisfies the hardness range for the standard peak-aged condition for 17-4 PH stainless steel (1 h at 482°C) [3]. Although the material solutionized for 60 min possessed a higher initial hardness in the H925 condition (495°C), the solution duration had little impact at higher aging temperatures.

Table 5.4: Comparison of austenite volume fraction and Vickers microhardness for various 4-hour aging heat treatments following a 30-min or 60-min solutionizing step for nitrogen atomized material processed on the EOS M280 system

	30 min Soln HT		60 min Soln HT	
	% $\gamma$	HVN	% $\gamma$	HVN
Post-Soln	24%	262 $\pm$ 22	22%	356 $\pm$ 10
Solutionized + Aged	495°C	22%	21%	335 $\pm$ 25
	550°C	21%	25%	377 $\pm$ 10
	580°C	24%	21%	402 $\pm$ 10
	620°C	20%	19%	419 $\pm$ 13
	650°C	19%	16%	417 $\pm$ 12
	680°C	17%	14%	419 $\pm$ 14
	720°C	19%	15%	418 $\pm$ 14
	760°C	16%	13%	388 $\pm$ 13

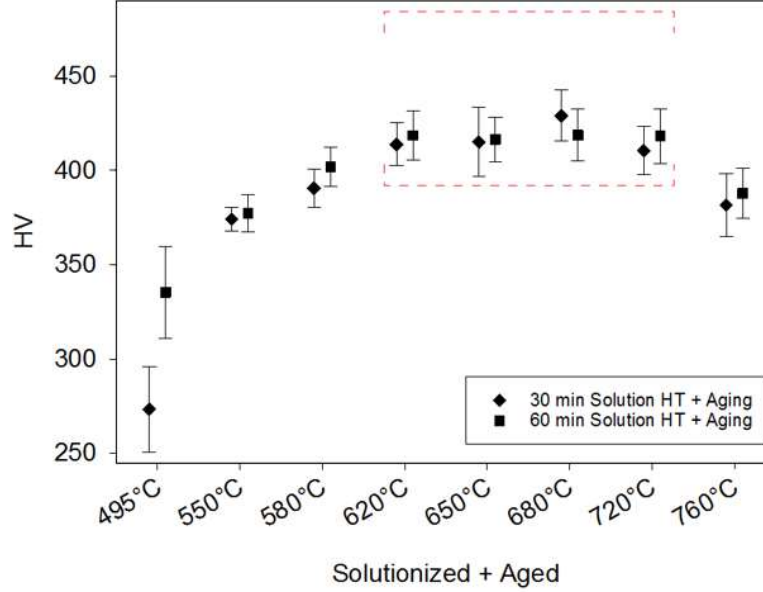


Figure 5.6: Vickers hardness measurements of highly austenitic feedstock fabricated under nitrogen, then solutionized for either 30 or 60 min followed by 4-hour aging, with specified hardness range for H900 peak age condition [3] indicated by brackets

### 5.5 Three-stage Heat Treatment: Homogenization + Solutionizing + Aging

Similar to solutionizing, the purpose of a homogenization step is to minimize elemental segregation within the microstructure. [68] A homogenization heat treatment often leads to reduced ferrite content and increases the likelihood of austenite transforming to martensite upon cooling. [9] Three-stage heat treatments were carried out along one of two paths: after an initial homogenization at 1150°C for 90 min, the intermediate 30 min solutionizing step was terminated either by the same air-cooling method used in the rest of this study or was rapidly cooled using a water quench. The air-cooled or water-quenched samples were then subjected to the same overaging heat treatments discussed in previous sections.

The results of the three-stage heat treatments—including measurements of the intermediate stages—for material fabricated on the 3D Systems ProX 200 are presented in Table 5.5. Unfortunately, the argon atomized components fabricated on this system lacked sufficient material to perform aging heat treatments within this category, so only intermediate conditions are provided. However, the low levels of retained austenite within these samples and the similarity to the solutionized state in Table 5.2 suggests the heat treatment response would be comparable to the two-stage heat treatment. Overall, the addition of a homogenization step did not significantly alter the aging conditions of the nitrogen atomized material. However, compared to the results in Section 5.3, Figure 5.7 indicates that the differences introduced by the processing gas were minimized. Also, following homogenization, variability in the hardness measurements of either solutionized state was lower than that observed in the two-stage heat treatment.

Initial three-stage heat treatment results for material fabricated on the EOS M280 are shown in Figure 5.8, with extended hardness properties representing the additional aging temperatures performed on the nitrogen atomized material displayed in Figure 5.9. The measured hardness values and retained austenite fractions are listed in Table 5.6. As observed with the 3D Systems builds, the addition of a homogenization step had little impact on the aging conditions of the primarily  $\alpha/\alpha'$  material. While the underaging and overaging trends still indicated a peak-aged condition around 680°C, maximum hardness was not observed at this condition. The additional complexity of applying a three-stage heat treatment introduced greater variability in the nitrogen atomized material on the EOS M280.



Table 5.5: Comparison of austenite volume fraction and Vickers microhardness following a three-stage heat treatment consisting of homogenization, a solutionizing step that terminated in either air-cooling or a water-quench, then 4-hour aging; fabricated on 3D Systems ProX 200

		Ar/Ar		Ar/N <sub>2</sub>		N <sub>2</sub> /Ar		N <sub>2</sub> /N <sub>2</sub>	
		% $\gamma$	HVN	% $\gamma$	HVN	% $\gamma$	HVN	% $\gamma$	HVN
Post-Homog.		3%	303 $\pm$ 7	2%	309 $\pm$ 8	7%	363 $\pm$ 7	13%	366 $\pm$ 10
Hom+Sol	Post-Soln (air)	<1%	301 $\pm$ 6	<1%	308 $\pm$ 10	1%	349 $\pm$ 7	1%	361 $\pm$ 6
	495°C	[insufficient material]				4%	398 $\pm$ 5	14%	392 $\pm$ 5
	580°C					20%	343 $\pm$ 5	19%	342 $\pm$ 5
	620°C					19%	327 $\pm$ 9	22%	321 $\pm$ 10
	+Aged								
Hom+Sol	Post-Soln (H <sub>2</sub> O)	0%	304 $\pm$ 11	<1%	297 $\pm$ 8	<1%	358 $\pm$ 6	4%	362 $\pm$ 8
	495°C	[insufficient material]				9%	397 $\pm$ 7	22%	397 $\pm$ 5
	580°C					21%	354 $\pm$ 6	13%	358 $\pm$ 5
	620°C					21%	314 $\pm$ 5	21%	319 $\pm$ 6
	+Aged								

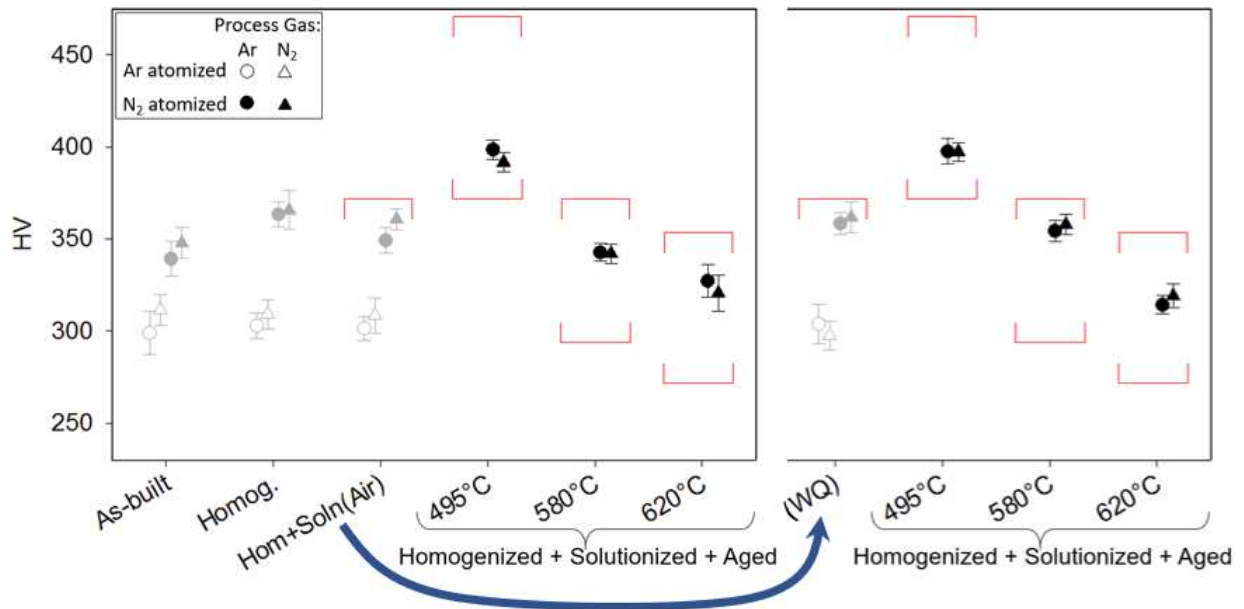


Figure 5.7: Comparison of austenite volume fraction and Vickers microhardness following a three-stage heat treatment consisting of homogenization, a solutionizing step that terminated in either air-cooling or a water-quench, then 4-hour aging; fabricated on 3D Systems ProX 200

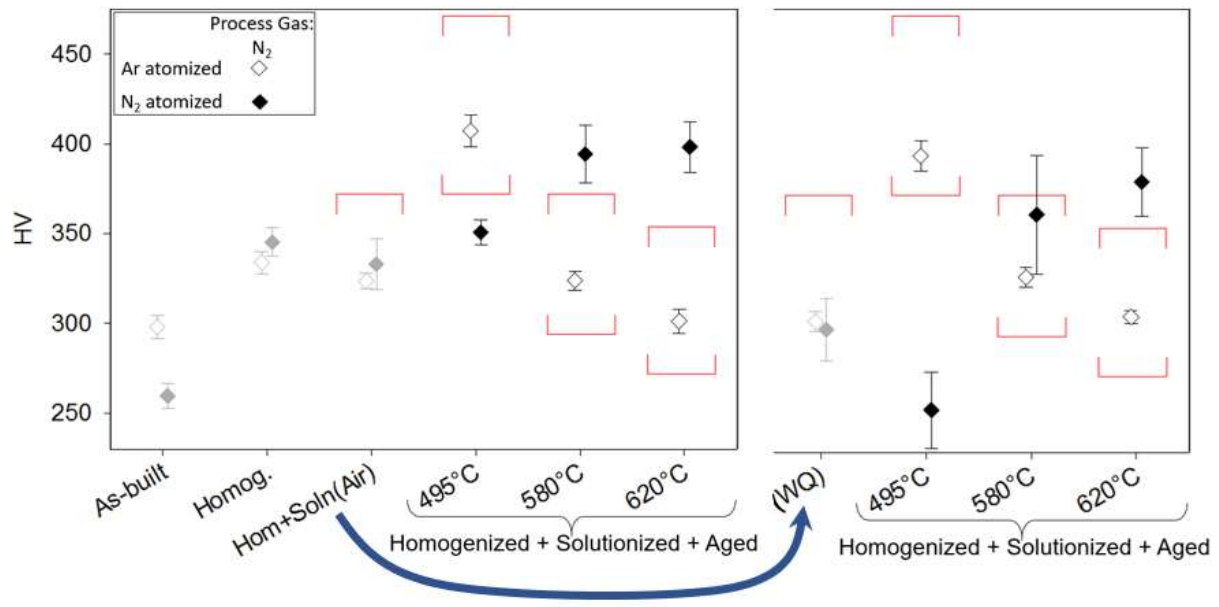


Figure 5.8: Comparison of austenite volume fraction and Vickers microhardness following a three-stage heat treatment consisting of homogenization, a solutionizing step that terminated in either air-cooling or a water-quench, then 4-hour aging; fabricated on EOS M280

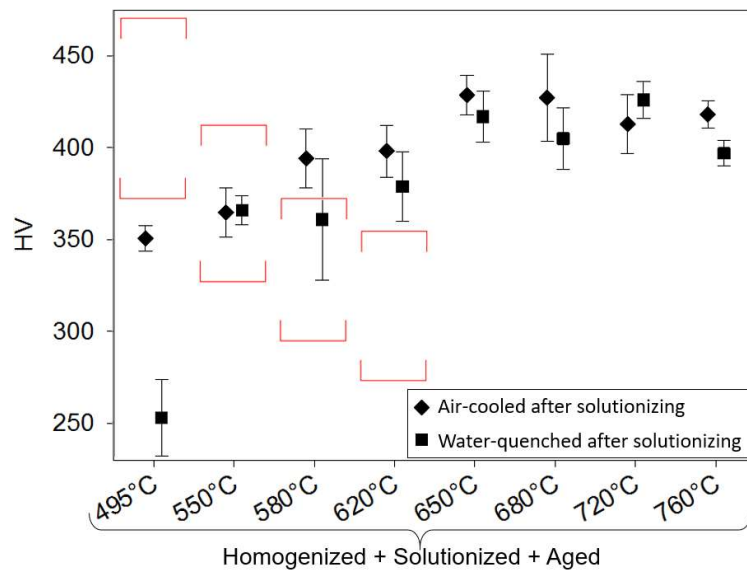


Figure 5.9: Comparison of austenite volume fraction and Vickers microhardness of highly austenitic feedstock fabricated on EOS M280, subjected to three-stage heat treatments

Table 5.6: Comparison of austenite volume fraction and Vickers microhardness following a three-stage heat treatment consisting of homogenization, a solutionizing step that terminated in either air-cooling or a water-quench, then 4-hour aging; fabricated on EOS M280

		EOS Ar/N <sub>2</sub>				EOS N <sub>2</sub> /N <sub>2</sub>			
		air-cool		water-quench		air-cool		water-quench	
		post solution		post solution		post solution		post solution	
		% $\gamma$	HVN	% $\gamma$	HVN	% $\gamma$	HVN	% $\gamma$	HVN
Post-Homog		<1%	334 $\pm$ 6	<1%	334 $\pm$ 6	31%	345 $\pm$ 8	31%	345 $\pm$ 8
Post-Soln		0%	324 $\pm$ 4	<1%	302 $\pm$ 6	25%	333 $\pm$ 14	25%	298 $\pm$ 17
Homog. + Solution + Aged	495°C	<1%	407 $\pm$ 9	<1%	394 $\pm$ 8	34%	351 $\pm$ 7	42%	253 $\pm$ 21
	550°C					20%	365 $\pm$ 13	17%	366 $\pm$ 8
	580°C	7%	324 $\pm$ 5	11%	327 $\pm$ 5	12%	394 $\pm$ 16	37%	361 $\pm$ 33
	620°C	5%	301 $\pm$ 7	5%	305 $\pm$ 4	18%	398 $\pm$ 14	37%	379 $\pm$ 19
	650°C					15%	429 $\pm$ 11	16%	417 $\pm$ 14
	680°C					12%	427 $\pm$ 24	31%	405 $\pm$ 17
	720°C					10%	413 $\pm$ 16	28%	426 $\pm$ 10
	760°C					10%	418 $\pm$ 8	8%	397 $\pm$ 7

## 5.6 Summary and Conclusions

The heat treatment response of additively manufactured 17-4 PH stainless steel, representing a range of retained austenite levels as dictated by the chemical composition, was investigated. The study focused on three overaging conditions specified for wrought [3] product: H925 (4h at 495°C), H1075 (4h at 580°C), and H1150 (4h at 620°C). Aging heat treatments were conducted as part of at least three independent paths: directly from the as-built condition, as part of a two-stage heat treatment following an initial solutionization, and finally, as part of a three-stage heat treatments that consisted of homogenization, solutionization, then aging. For the three-stage heat treatments, the intermediate solutionizing step was terminated either by water quench or permitted to air-cool.

When aged directly from the as-built condition, the heat treatment response is highly dependent on the amount of retained austenite in the material. A solutionizing heat treatment

significantly reduced austenite levels, and among materials with  $\leq 4\%$  austenite, generally satisfied hardness requirements upon aging. However, the highly austenitic material sustained an aberrant behavior, and did not exhibit peak-aging until approximately 4 hours at 680°C. The addition of a homogenization step had little impact on the aging response.

## Chapter 6

### SUMMARY

#### 6.1 Primary Conclusions

The role of feedstock atomization and shielding gas on the heat treat response of AM 17-4 PH stainless steel was investigated. Four feedstock powders representing a range of nitrogen levels were used to fabricate components under either a nitrogen or argon atmosphere. The resulting chemical compositions were used to explain differences in phase proportions by simulating solidification and martensite start temperatures. As more nitrogen led to greater levels of retained austenite, the heat treatment response deviated from the expected trend, as noted in the following observations:

- The atomization condition (and to a lesser extent, the choice of shielding gas) affect the concentration of nitrogen in AM 17-4 PH stainless steel. Argon atomized feedstocks contained only 0.01 wt.% N, while the concentration increased to levels of 0.06 to 0.12 wt.% in nitrogen atomized powders. Nitrogen content within AM builds was 0 to 0.03 wt.% higher than in the feedstock. Higher nitrogen levels corresponded to increased levels of retained austenite.
- For all conditions, higher austenite levels were observed in the feedstocks than in the fabricated components. Material fabricated from argon atomized feedstock was fully ferritic/martensitic regardless of processing gas, while the nitrogen atomized feedstock maintained moderate levels of retained austenite.
- When aged directly from the as-built condition, the heat treatment response is influenced by the amount of retained austenite. Primarily ferritic/martensitic materials followed the expected overaged trend of declining hardness values with increasing temperatures. While partially austenitic materials also followed this trend at low overaging temperatures, hardness increased at higher temperatures. Once austenite levels were further reduced following a solutionizing heat treatment, materials with  $\leq 4\%$  austenite generally satisfied hardness requirements upon aging.
- For primarily austenitic material, the lowest hardness values were observed following an overaging heat treatment closest to the conventional peak age condition for 17-4 PH grade stainless steel, and contrary to the expected overaging trend, continued to increase at higher aging temperatures. Although solutionizing reduced the austenite level to  $< 30\%$ , a peak aged condition was not observed until 4 hr at 680°C.

- While preceding aging heat treatments with a solutionizing step generally improved the heat treatment response, preceding it with a homogenization step (90 min at 1150°C) had little impact

## **6.2 Potential Next Steps**

While part of this study focused on thermally induced martensitic transformation, mechanical testing would reveal how higher retained austenite levels impact strain induced martensitic transformation as well. In addition, the projected martensite start ( $M_s$ ) temperatures calculated for the different compositions could be compared to empirical data through quenching dilatometry experiments.

## REFERENCES

- [1] AK Steel product data bulletin, 17-4 PH Stainless Steel, (n.d.).  
[http://www.aksteel.com/pdf/markets\\_products/stainless/precipitation/17-4\\_PH\\_Stainless\\_Steel\\_PDB\\_201512.pdf](http://www.aksteel.com/pdf/markets_products/stainless/precipitation/17-4_PH_Stainless_Steel_PDB_201512.pdf) (accessed August 1, 2017).
- [2] R. Bhambroo, S. Roychowdhury, V. Kain, V.S. Raja, Effect of reverted austenite on mechanical properties of precipitation hardenable 17-4 stainless steel, *Mater Sci Eng A*. 568 (2013) 127–133. doi:10.1016/j.msea.2013.01.011.
- [3] ASTM Standard A693, Standard Specification for Precipitation-Hardening Stainless and Heat-Resisting Steel, Plate, Sheet, and Strip, (2013). doi:10.1520/A0564\_A0693-13.
- [4] C.N. Hsiao, C.S. Chiou, J.R. Yang, Aging reactions in a 17-4 PH stainless steel, *Mater Chem Phys*. (2002). doi:10.1016/S0254-0584(01)00460-6.
- [5] F.C. Campbell, ed., *Elements of Metallurgy and Engineering Alloys*, ASM International, 2008.
- [6] M. Mahmoudi, A. Elwany, A. Yadollahi, S.M. Thompson, L. Bian, N. Shamsaei, Mechanical properties and microstructural characterization of selective laser melted 17-4 PH stainless steel, *Rapid Prototyp J.* (2017). doi:10.1108/RPJ-12-2015-0192.
- [7] A. Ziewiec, A. Zielińska-Lipiec, E. Tasak, Microstructure of welded joints of X5CrNiCuNb 16-4 (17-4 PH) martensitic stainless steel after heat treatment, *Arch Metall Mater.* 59 (2014) 965–970. doi:10.2478/amm-2014-0162.
- [8] W. Liu, J. Ma, M.M. Atabaki, R. Pillai, B. Kumar, U. Vasudevan, H. Sreshta, R. Kovacevic, Hybrid Laser-arc Welding of 17-4 PH Martensitic Stainless Steel, *Lasers Manuf Mater Process.* 2 (2015) 74–90. doi:10.1007/s40516-015-0007-2.
- [9] J.C. Lippold, D.J. Kotecki, *Welding Metallurgy and Weldability of Stainless Steels*, John Wiley & Sons, 2005.
- [10] A.L. Schaeffler, Constitution Diagram for Stainless Steel Weld Metal, *Met Prog.* 56 (1949) 680–680B.
- [11] V. Kujanpää, N. Suutala, T. Takalo, T. Moisio, Correlation between solidification

- cracking and microstructure in austenitic and austenitic-ferritic stainless steel welds, *Weld Res Int.* 9.2 (1979) 55–75.
- [12] I. Masumoto, K. Tamaki, M. Kutsuna, Hot Cracking of Austenitic Steel Weld Metal, *J Japan Weld Soc.* 41 (1972) 1306–1314.
  - [13] H. Thier, Delta-Ferrit und Heißrisse beim Schweißen chemisch beständiger austenitischer Stähle, *DVS-Berichte.* 41 (1976) 100–104.
  - [14] J.M. Vitek, A. Dasgupta, S.A. David, Microstructural Modification of Austenitic Stainless Steels By Rapid Solidification., *Metall Trans A, Phys Metall Mater Sci.* 14 A (1983) 1833–1841. doi:10.1007/BF02645553.
  - [15] S.A. David, J.M. Vitek, R.W. Reed, T.L. Hebble, Effect of rapid solidification on stainless steel weld metal microstructures and its implications on the Schaeffler diagram, Oak Ridge, TN, 1987. doi:10.2172/5957599.
  - [16] J.W. Elmer, S.M. Allen, T.W. Eagar, The Influence of Cooling Rate on the Ferrite Content of Stainless Steel Alloys, *Proc 2nd Int Conf Trends Weld Res.* (1989) 165–170.
  - [17] T. Debroy, H.L. Wei, J.S. Zuback, T. Mukherjee, J.W. Elmer, J.O. Milewski, A.M. Beese, A. Wilson-heid, A. De, W. Zhang, Progress in Materials Science Additive manufacturing of metallic components – Process , structure and properties, *Prog Mater Sci.* 92 (2018) 112–224. doi:10.1016/j.pmatsci.2017.10.001.
  - [18] D.D. Gu, W. Meiners, K. Wissenbach, R. Poprawe, Laser additive manufacturing of metallic components: materials, processes and mechanisms, *Int Mater Rev.* 57 (2012) 133–164. doi:10.1179/1743280411Y.0000000014.
  - [19] Y. Matsuoka, T. Iwasaki, N. Nakada, T. Tsuchiyama, S. Takaki, Effect of Grain Size on Thermal and Mechanical Stability of Austenite in Metastable Austenitic Stainless Steel, *ISIJ Int.* (2013). doi:10.2355/isijinternational.53.1224.
  - [20] S. Takaki, K. Fukunaga, J. Syarif, T. Tsuchiyama, Effect of Grain Refinement on Thermal Stability of Metastable Austenitic Steel, *Mater Trans.* (2004). doi:10.2320/matertrans.45.2245.



- [21] Z. Sun, X. Tan, S.B. Tor, W.Y. Yeong, Selective laser melting of stainless steel 316L with low porosity and high build rates, (2016). doi:10.1016/j.matdes.2016.05.035.
- [22] X.M. Zhao, J. Xu, X.X. Zhu, S.M. Zhang, W.D. Zhao, G.L. Yuan, Characterization of 17-4PH stainless steel powders produced by supersonic gas atomization, *Int J Miner Metall Mater.* (2012). doi:10.1007/s12613-012-0519-0.
- [23] R.M. German, *Powder Metallurgy and Particulate Materials Processing*, Metal Powders Industries Federation, Princeton, NJ, 2005.
- [24] C.J. Long, W.T. Delong, *The Ferrite Content of Austenitic Stainless Steel Weld Metal*, (1973).
- [25] C. Bodsworth, *Physical Chemistry of Iron and Steel Manufacture*, Longmans, 1963.
- [26] E.A. Ul'yanin, N.A. Sorokina, Y.M. Zaretskii, Properties of austenitic steel with nickel and nitrogen at low temperatures, *Met Sci Heat Treat.* (1969). doi:10.1007/BF00653157.
- [27] H.F. Ebling, M.A. Scheil, *Advances in the Technology of Stainless Steels and Related Alloys*, ASTM-STP, 1965.
- [28] H.E. McGannon, *The Making, Shaping and Treating of Steel*, 1971.
- [29] I. Shuro, S. Kobayashi, T. Nakamura, K. Tsuzaki, Determination of  $\alpha/\gamma$  phase boundaries in the Fe-Cr-Ni-Mn quaternary system with a diffusion-multiple method, *J Alloys Compd.* (2014). doi:10.1016/j.jallcom.2013.11.095.
- [30] Q. Wang, B. Zhang, K. Yang, Thermodynamic Calculation Study on Effect of Manganese on Stability of Austenite in High Nitrogen Stainless Steels, *Metall Mater Trans A Phys Metall Mater Sci.* (2016). doi:10.1007/s11661-016-3532-5.
- [31] V. Raghavan, Effect of manganese on the stability of austenite in Fe-Cr-Ni alloys, *Metall Mater Trans A.* (1995). doi:10.1007/BF02664662.
- [32] A.P. Gulyaev, A.P. Shlyamnev, N.A. So, *Stainless Steels Effect on Alloying on the Martensitic Transformation in Stainless Steels*, (n.d.).
- [33] ASTM Standard A564/A564M, *Standard Specification for Hot-Rolled and Cold-Finished Age-Hardening Stainless Steel Bars and Shapes*, (2013). doi:10.1520/A0564\_A0564M-13.

- [34] L.E. Murr, E. Martinez, J. Hernandez, S. Collins, K.N. Amato, S.M. Gaytan, P.W. Shindo, Microstructures and properties of 17-4 PH stainless steel fabricated by selective laser melting, *J Mater Res Technol.* (2012). doi:10.1016/S2238-7854(12)70029-7.
- [35] M. Murayama, K. Hono, Y. Katayama, Microstructural evolution in a 17-4 PH stainless steel after aging at 400 °C, *Metall Mater Trans A.* (1999). doi:10.1007/s11661-999-0323-2.
- [36] H.K. Rafi, D. Pal, N. Patil, T.L. Starr, B.E. Stucker, Microstructure and Mechanical Behavior of 17-4 Precipitation Hardenable Steel Processed by Selective Laser Melting, *J Mater Eng Perform.* (2014). doi:10.1007/s11665-014-1226-y.
- [37] T. LeBrun, T. Nakamoto, K. Horikawa, H. Kobayashi, Effect of retained austenite on subsequent thermal processing and resultant mechanical properties of selective laser melted 17-4 PH stainless steel, *Mater Des.* 81 (2015) 44–53. doi:10.1016/j.matdes.2015.05.026.
- [38] L. Facchini, N. Vicente, I. Lonardelli, E. Magalini, P. Robotti, M. Alberto, Metastable austenite in 17-4 precipitation-hardening stainless steel produced by selective laser melting, *Adv Eng Mater.* (2010). doi:10.1002/adem.200900259.
- [39] M. Averyanova, P. Bertrand, B. Verquin, Effect of Initial Powder Properties on Final Microstructure and Mechanical Properties of Parts Manufactured By Selective Laser Melting, in: B. Katalinic (Ed.), *Proc 21st Int DAAAM Symp*, DAAAM International, Vienna, Austria, EU, 2010.
- [40] T.L. Starr, K. Rafi, B. Stucker, C.M. Scherzer, Controlling Phase Composition in Selective Laser Melted Stainless Steels, in: *Proc Solid Free Fabr Symp*, 2012: pp. 439–456.
- [41] S. Cheruvathur, E.A. Lass, C.E. Campbell, Additive Manufacturing of 17-4 PH Stainless Steel: Post-processing Heat Treatment to Achieve Uniform Reproducible Microstructure, *JOM.* 68 (2016) 930–942. doi:10.1007/s11837-015-1754-4.
- [42] M.R. Stoudt, R.E. Ricker, E.A. Lass, L.E. Levine, Influence of Postbuild Microstructure on the Electrochemical Behavior of Additively Manufactured 17-4 PH Stainless Steel,

- JOM. (2017). doi:10.1007/s11837-016-2237-y.
- [43] B. Clausen, D.W. Brown, J.S. Carpenter, K.D. Clarke, A.J. Clarke, S.C. Vogel, J.D. Bernardin, D. Spernjak, J.M. Thompson, Deformation behavior of additively manufactured GP1 stainless steel, *Mater Sci Eng A*. 696 (2017) 331–340. doi:10.1016/j.msea.2017.04.081.
  - [44] SAE International Aerospace Material Specification, Steel, Corrosion Resistant, Investment Castings 16Cr - 4.1 Ni - 0.28Cb - 3.2Cu Homogenization and Solution Heat Treated or Homogenization, Solution, and Precipitation Heat Treated, (2015). [www.sae.org](http://www.sae.org).
  - [45] ASTM Standard E1019, Standard Test Methods for Determination of Carbon, Sulfur, Nitrogen, and Oxygen in Steel, Iron, Nickel, and Cobalt Alloys by Various Combustion and Fusion Techniques, (2011). doi:10.1520/E1019-11.
  - [46] ASTM Standard E1479, Standard Practice for Describing and Specifying Inductively Coupled Plasma, (2016). doi:10.1520/E1479-16.
  - [47] ASTM Standard B213, Standard Test Methods for Flow Rate of Metal Powders Using the Hall Flowmeter Funnel, (n.d.). doi:10.1520/B0213-13.
  - [48] ASTM Standard B212, Standard Test Method for Apparent Density of Free-Flowing Metal Powders Using the Hall Flowmeter Funnel, (2013). doi:10.1520/B0212-13.
  - [49] ASTM Standard B527, Standard Test Method for Tap Density of Metal Powders and Compounds, (2015). doi:10.1520/B0527-15.
  - [50] L.F. Pease, W.G. West, *Fundamentals of Powder Metallurgy*, Metal Powder Industries Federation, 2002.
  - [51] M.. Balmforth, J.C. Lippold, A New Ferritic-Martensitic Stainless Steel Constitution Diagram, *Weld J*. (2000) 339–345.
  - [52] J.C. Polidoro, A.F. Alves Medeiros, R.P. Xavier, J.A. Medeiros, R.M. Boddey, B.J. Rodrigues Alves, S. Urquiaga, Evaluation of techniques for determination of molybdenum in sugarcane leaves, *Commun Soil Sci Plant Anal*. 37 (2006) 77–91.

doi:10.1080/00103620500408753.

- [53] ASTM Standard E975, Standard Practice for X-Ray Determination of Retained Austenite in Steel with Near Random Crystallographic Orientation, (2013). doi:10.1520/E0975-13.
- [54] Y. Waseda, E. Matsubara, K. Shinoda, X-Ray Diffraction Crystallography, Springer, Berlin, 2011. doi:10.1007/978-3-642-16635-8.
- [55] Y.M. Mos, A.C. Vermeulen, C.J.N. Buisman, J. Weijma, Y.M. Mos, A.C. Vermeulen, C.J.N. Buisman, J. Weijma, X-Ray Diffraction of Iron Containing Samples : The Importance of a Suitable Configuration X-Ray Diffraction of Iron Containing Samples : The Importance of a Suitable, Geomicrobiol J. 35 (2018) 511–517. doi:10.1080/01490451.2017.1401183.
- [56] B.D. Cullity, S.R. Stock, Elements of X-Ray Diffraction, 3rd ed., Prentice Hall, Upper Saddle River, NJ, 2001.
- [57] L. Cheng, A. Böttger, T.H. de Keijser, E.J. Mittemeijer, Lattice Parameters of Iron-Carbon and Iron-Nitrogen Martensites and Austenites, Scr Metall Mater. 24.3 (1990) 509–514.
- [58] ASTM Standard E1097, Standard Guide for Determination of Various Elements by Direct Current Plasma Atomic Emission Spectrometry, (2012). doi:10.1520/E1097-12.
- [59] A.B. Greninger, A.R. Troiano, The martensite thermal arrest in iron-carbon alloys and plain carbon steels, Trans Am Soc Met. 30 (1942) 1–26.
- [60] M.J. Bibby, J.G. Parr, The Martensitic Transformation in Pure Iron, J Iron Steel Inst. 202 (1964) 100–104.
- [61] J.V. Russell, F.T. McGuire, A Metallographic Study of the Decomposition of Austenite in Manganese Steels, Trans Am Soc Met. 33 (1944).
- [62] G. Ghosh, G.B. Olson, Computational thermodynamics and the kinetics of martensitic transformation, J Phase Equilibria. 22.3 (2001) 199–207.
- [63] ASTM Standard E140, Standard Hardness Conversion Tables for Metals Relationship Among Brinell Hardness, Vickers Hardness, Rockwell Hardness, Superficial Hardness, Knoop Hardness, Scleroscope Hardness, and Leeb Hardness, (2013). doi:10.1520/E0140-

12B.

- [64] ASTM Standard E407, Standard Practice for Microetching Metals and Alloys, (2015). doi:10.1520/E0407-07R15E01.
- [65] R. Abbaschian, L. Abbaschian, R.E. Reed-Hill, Physical Metallurgy Principles, Fourth, Cengage Learning, Stamford, CT, 2009.
- [66] K.M. Coffy, Microstructure and Chemistry Evaluation of Direct Metal Laser Sintered 15-5 Stainless Steel, University of Central Florida, 2014.
- [67] J. Wang, H. Zou, C. Li, S. yu Qiu, B. lu Shen, The effect of microstructural evolution on hardening behavior of type 17-4PH stainless steel in long-term aging at 350 C, Mater Charact. 57 (2006) 274–280. doi:10.1016/j.matchar.2006.02.004.
- [68] A. Murthy, S. Lekakh, V. Richards, D. Van Aken, Microstructure and properties of NB, v and N modified CB7CU-1 (17-4 PH) steel, Int J Met. (2010). doi:10.1007/BF03355466.